Retrieval of aerosol properties from Airborne Hyper Angular Rainbow Polarimeter (AirHARP) observations during ACEPOL 2017

Anin Puthukkudy[1,2,3], J. Vanderlei Martins[1,2,3], Lorraine A. Remer[2,3], Xiaoguang Xu[2,3], Oleg Dubovik[4], Pavel Litvinov[5], Brent McBride[1,2,3], Sharon Burton[6], and Henrique M. J. Barbosa[7]

[1]Physics Department, University of Maryland Baltimore County, Baltimore, 21250, USA,
[2]Joint Center for Earth Systems Technology, University of Maryland Baltimore County, 5523 Research Park DR, Baltimore, MD 21228, USA)
[3]Earth and Space Institute, University of Maryland Baltimore County, MD, USA
[4]Laboratoire d'Optique Atmosphérique, CNRS/Université Lille, Villeneuve d'Ascq, France
[5]GRASP-SAS, Villeneuve d'Ascq, France
[6]NASA Langley Research Center, Hampton, VA, 23681, USA
[7]Instituto de Física, Universidade de São Paulo., São Paulo, Brazil

Correspondence to: Anin Puthukkudy (aputhukkudy@umbc.edu)

Abstract. Multi-angle polarimetric (MAP) imaging of Earth scenes can be used for the retrieval of microphysical and optical parameters of aerosols and clouds. The Airborne Hyper-Angular Rainbow Polarimeter (AirHARP) is an aircraft MAP instrument with the hyper-angular imaging capability of 60 along-track viewing angles at 670 nm, and 20 along-track viewing angles at other wavelengths 440, 550, 870 nm across the full 114˚(94˚) along-track (cross-track) field-of-view. Here we report the retrieval of aerosol properties using the Generalized Retrieval of Aerosols and Surface Properties (GRASP) algorithm applied to AirHARP observations collected during the NASA Aerosol Characterization from Polarimeter and Lidar (ACEPOL) campaign in October – November 2017. The retrieved aerosol properties include spherical fraction (SF), aerosol volume concentration in multiple size distribution modes, and with sufficient aerosol loading, complex aerosol refractive index. From these primary retrievals, we derive aerosol optical depth (AOD), Angstrom exponent (AE), and single scattering albedo (SSA). AOD retrieved from AirHARP measurements are compared with the High Spectral Resolution LiDAR-2 (HSRL2) AOD measurements at 532 nm and validated with measurements from collocated Aerosol Robotic NETwork (AERONET) stations. A good correlation with HSRL2 (ρ = 0.940, $|BIAS|$ = 0.062) and AERONET AOD (0.013 ≤ Mean Absolute Error (MAE) ≤ 0.017, 0.013 ≤ $|BIAS|$ ≤ 0.017) measurements is observed for the collocated points. Forest fire smoke intercepted during ACEPOL provided a situation with sufficient aerosol loading to retrieve the real part of the refractive index (RRI) of 1.55 and the imaginary part of the refractive index (IRI) of 0.024 The derived SSAs for this case are 0.87, 0.86, 0.84, 0.81 at wavelengths of 440 nm, 550 nm, 670 nm, and 870 nm, respectively. Finer particles with an average AE of 1.53, volume median radius of 0.157 µm and standard deviation of 0.55 µm for fine mode is observed for the same smoke plume. These results serve as a proxy for the scale and detail of aerosol retrievals that are anticipated from future space mission data, as :HARP CubeSat (mission begins 2020) and HARP2 (aboard the NASA PACE mission with launch in 2023) are near duplicates of AirHARP and are expected to provide the same level of aerosol characterization.

1 Introduction

35   Aerosols play an important role in Earth's climate (Boucher et al., 2013; Hobbs, 1993; Kaufman et al., 2002; Koren et al., 2004): they directly perturb Earth's radiation budget and indirectly modify cloud properties, which in turn influence the planet's energy and hydrological budgets (Lenoble et al., 2013; Penner et al., 2001). The *direct radiative effects* of aerosols, the absorption and scattering of light, depend on the intrinsic optical properties of the particles, the total aerosol loading and the radiative properties of the surface beneath the aerosol layer. Aerosols are highly variable, both in their spatial and temporal

40   distributions, but also in their optical and microphysical properties; it is especially challenging to represent their radiative effect realistically in climate models (Dubovik et al., 2002; Masmoudi et al., 2003). Therefore, aerosol radiative forcing remains one of the main uncertainties in global climate change estimation (Boucher et al., 2013; Chen and Penner, 2005; Hansen et al., 2011; Penner et al., 2011). Furthermore, aerosols are a mixture of sub-millimeter, suspended particles with different sizes, morphology, and composition that result in complex physical, chemical and optical properties (Kahnert, 2010; Kokhanovsky

45   et al., 2015; Tanré et al., 2011). To better characterize the aerosol role in the global radiation budget and narrow uncertainties in predicting climate change, we need to better understand and constrain the temporal and spatial distributions of these properties. In addition, a careful understanding of aerosol properties is essential for air quality monitoring/mitigation, characterizing fertilization of ecosystems, hydrological forecasting, etc. (Shiraiwa et al., 2017; Westberry et al., 2019).

The last few decades have seen unprecedented efforts to better characterize aerosol particle properties and aerosol radiative

50   effects with in situ and remote sensing observations. For example, in situ measurements based on a wide variety of techniques, such as photoacoustic and cavity ring-down spectrometers, filter-based photometers, and polarized imaging nephelometers have provided detailed information on size, shape, and absorption for many different regions across the world, and continue to do so (Bergstrom et al., 2007; Bond et al., 1999; Dubovik et al., 2000; Espinosa et al., 2017, 2018; Moosmüller et al., 2005; Petzold et al., 2005; Rocha-Lima et al., 2014; Snider et al., 2015). However, in situ measurements have limitations due to the

55   small sampling volumes that they represent and very limited in number and spatial coverage. In addition to in situ instruments, ground-based remote sensing networks, primarily the AErosol RObotic NETwork (AERONET), provide much larger coverage over the continental Earth (Holben et al., 1998, 2001). These AERONET observations measure downwelling direct sunlight, and from these measurements, it is possible to obtain highly accurate spectral aerosol optical depth (AOD), defined as the integration of the aerosol extinction over the entire atmospheric column. In addition, AERONET instruments measure diffused

60   and polarized sky radiance, from which columnar particle optical and microphysical properties are retrieved (Dubovik et al., 2006; Dubovik and King, 2000; Xu and Wang, 2015). AERONET instruments are widespread but are not truly global.

In order to achieve seamless global coverage, we need to rely on satellite remote sensing to characterize the global aerosol system, including particle properties. Most aerosol products retrieved from satellite instrument data are limited to AOD or qualitative aerosol type (Diner et al., 2008; Kahn et al., 2009; Lenoble et al., 2013; Levy et al., 2013; Limbacher and Kahn,

65   2019; Martonchik et al., 2002). Whereas, a Multi-Angle Polarimeter (MAP) have enough information content to retrieve particle properties with a greater degree of accuracy (Dubovik et al., 2011; Hasekamp and Landgraf, 2007; Knobelspiesse et

al., 2012; Mischenko et al., 2002; Mishchenko and Travis, 1997). A MAP instrument looks at Earth scenes at different viewing angles and measures the angular scattering and polarization of reflected light after interacting with Earth's surface, atmospheric molecules, clouds, and aerosols. Using multiple polarization angles and multiple wavelengths (if available), the aerosol signal

70   can be isolated from the signals coming from the atmosphere and the surface beneath. Furthermore, these algorithms can invert MAP measurements to obtain optical properties of the aerosol within a significant level of certainty. This capability has been demonstrated by space-borne POLDER I, II and III (POLarization and Directionality of the Earth's Reflectance) (Deuzé et al., 1999, 2001; Dubovik et al., 2019; Goloub et al., 1999; Leroy et al., 1997), and will be continued by the Multi-viewing multi-channel multi-polarisation imager (3MI): a future MAP instrument from the POLDER heritage scheduled to launch in 2021

75   (Fougnie et al., 2018). Currently, there are several modern MAP concepts that demonstrate technological advancements relative to the original POLDER, designed specifically as proxies for future spaceborne missions. These include, in addition to 3MI, Research Scanning Polarimeter (RSP) (Cairns et al., 1999, 2003), Airborne Multiangle Spectro Polarimetric Imager (AirMSPI) (Diner et al., 2013), SPEX Airborne (Smit et al., 2019), Observing System Including PolaRisation in the Solar Infrared Spectrum (OSIRIS) which is a 3MI airborne simulator, and Hyper-Angular Rainbow Polarimeter (HARP) (Martins

80   et al., 2018; Mcbride et al., 2020). For a comprehensive review of the polarimetric remote sensing of atmospheric aerosols based on MAPs, we encourage the readers to refer to several reviews in the literature (Dubovik et al., 2019; Kokhanovsky et al., 2015; Remer et al., 2019). In this work, we focus on retrieval of aerosol properties using AirHARP data, the airborne version of HARP, from the NASA aircraft campaign, Aerosol Characterization from Polarimeter and Lidar (ACEPOL). We apply an inversion algorithm to AirHARP polarized measurements of the same target at different viewing angles and

85   wavelengths. The specific inversion algorithm is Generalized Retrieval of Aerosols and Surface Properties (GRASP) (Dubovik et al., 2011, 2014).

In Section 2, we provide a theoretical background for the measurements of multi-angle polarimetry and the inversion of those measurements to retrieve aerosol properties, and then describe the AirHARP instrument specifically, define the measuring geometry, and introduce the specific campaign when the measurements were made. Section 3 describes the GRASP retrieval

90   after covering the preliminary work preparing measurements for retrieval, including gas corrections. The results of applying GRASP to AirHARP measurements, including comparisons to collocated High Spectral Resolution LiDAR - 2 (HSRL2) and AERONET, are shown and discussed in Section 4 and 5. Section 6 discusses future research directions. Finally, Section 7 offers a conclusion. In addition, we provide two appendices. One details the land and ocean surface models that are essential to the GRASP inversion of aerosol, and the second one describes the calculation of aerosol optical depth from retrieved aerosol

95   particles.

2 Background

2.1 Theoretical basis of the measurements and retrieval

MAP instruments measure radiances at different viewing angles, polarization angles, and spectral bands. The state of polarization of measured light can be represented by the Stokes vector, $\mathbf{S}$, where the transpose of the vector is given as $\mathbf{S^T} = [\ S_0\ \ S_1\ \ S_2\ \ S_3]$ (Schott, 2009). The elements in the Stokes vector are,

$$\begin{bmatrix} S_0 \\ S_1 \\ S_2 \\ S_3 \end{bmatrix} = \begin{bmatrix} E_\parallel E_\parallel + E_\perp E_\perp \\ E_\parallel E_\parallel^* - E_\perp E_\perp^* \\ E_\parallel E_\perp^* + E_\perp E_\parallel^* \\ i\left(E_\parallel E_\perp^* - E_\perp E_\parallel^*\right) \end{bmatrix} \tag{1.1}$$

Where $E_\perp$ and $E_\parallel$ are the perpendicular and parallel components of the electric field $\vec{\mathbf{E}}$ respectively. The first element (S_o) represents the total radiance. The second and third elements (S_1, S_2) represent the linear polarization of the radiance, and the fourth element (S_3) represents circular polarization. Passive remote sensors, like AirHARP, use the sun as their light source. Therefore, sunlight incident on the atmosphere is defined as:

$$\mathbf{S}_{\mathbf{Inc}}^{T} = [S_0 \quad 0 \quad 0 \quad 0]. \tag{1.2}$$

Since the light from the sun is unpolarized, S_1, S_2, and S_3 of the Stokes vector are zero. The Stokes vector of the scattered light back into the instrument sensor is given by,

$$\mathbf{S}_{\mathbf{sca}}^{\mathbf{T}} = [S_{0_{sca}} \quad S_{1_{sca}} \quad S_{2_{sca}} \quad 0] \tag{1.3}$$

where the light reaching the instrument sensor has now acquired some polarization but is assumed to be only linearly polarized, an assumption that holds well for the Earth's atmosphere and surface (Dubovik et al., 2011; Kokhanovsky et al., 2015). In this paper, we use reduced radiances $I = \frac{\pi S_{0_{sca}}}{F_0}$, $Q = \frac{\pi S_{1_{sca}}}{F_0}$, and $U = \frac{\pi S_{2_{sca}}}{F_0}$ to define the Stokes vector of the scattered light measured by the MAP with I, Q, U notation. F_0 is the solar radiance ($\mathrm{W}m^{-2}\mu m^{-1}$) and hence I, Q, and U are dimensionless variables. I is the total radiation measured by MAP, the same that would be measured by a radiometer normalized by F_0/π. Q and U define orthogonal states of linear polarization and together, they form the *polarized intensity*, defined as (Schott, 2009),

$$P = \sqrt{Q^2 + U^2} \tag{1.4}$$

and the degree of linear polarization (*DoLP*) is

$$DoLP = P/I \tag{1.5}$$

2.2 AirHARP (Airborne Hyper Angular Rainbow Polarimeter)

The Hyper Angular Rainbow Polarimeter (HARP) is a modern MAP concept capable of wide Field-of-View (FOV), multi-angle, multi-wavelength polarimetric imagery of a ground scene even from a low-cost, CubeSat-size platform. The HARP program was initially funded by the NASA Earth Science and Technology Office (ESTO) InVEST program as a joint collaboration between the University of Maryland, Baltimore County (UMBC) in Baltimore, MD and the Space Dynamics

Laboratory at Utah State University in Logan, Utah. There are currently three instruments based on the original HARP concept:

120 HARP CubeSat, a self-contained space technology demonstration mission launched to the International Space Station in November 2019 for a year-long mission beginning in February 2020; HARP2, a payload instrument for NASA's Plankton, Aerosols, Clouds, ocean Ecosystem (PACE) mission set to launch in the early 2023s (Werdell et al., 2019); and AirHARP, an airborne version of the HARP concept. In this paper, we focus on aerosol retrievals derived from measurements made from AirHARP as a proxy for these future space missions.

125 AirHARP's swath spans an angle of 114° along-track and 94° in cross-track; a simulated cross-section image of the AirHARP instrument is shown in Fig. 1(a). It uses a Phillips prism system that splits the incoming beam of light into three components so that the radiation can be measured at three polarization angles simultaneously, with no moving parts. These polarization states are imaged on three CCD imaging sensors, denoted by A, B, and C, which measure the light at angles of linear polarization (AoLP) = 0°, 45°, and 90°, respectively, which are hereby denoted as I_A, I_B and I_C radiances. AirHARP has three

130 wavelengths (440 nm, 550 nm, and 870 nm) that measure at 20 along-track view angles plus a hyper-angle measurement at the 670 nm wavelength that measures at 60 along-track view angles (See Table 1). This capability allows AirHARP to view a single ground target from up to 60 different perspectives, and measure the angular scattering response emanating from that location in both total and polarized radiances. These radiances are measured in all four channels, and each collocated detector pixel, which corresponds to a single channel and view angle, is calibrated independently for the radiometric and polarimetric

135 measurements.

Using the calibration matrix $\mathbf{C}$ and measured I_A, I_B and I_C; the S_0, S_1 and S_2 elements of the Stokes vector are calculated using Eq. 2.1 (Fernandez-Borda et al., 2009) and subsequently reduced radiances I, Q and U for each collocated detector pixel.

$$\begin{bmatrix} S_{0_{\text{sca}}} \\ S_{1_{\text{sca}}} \\ S_{2_{\text{sca}}} \end{bmatrix} = \begin{bmatrix} C_{11} & C_{12} & C_{13} \\ C_{21} & C_{22} & C_{23} \\ C_{31} & C_{32} & C_{33} \end{bmatrix} \begin{bmatrix} I_A \\ I_B \\ I_C \end{bmatrix} \qquad (2.1)$$

The calibration matrix, $\mathbf{C}$, is derived from a laboratory calibration scheme described in Fernandez-Borda et al., 2009. The

140 AirHARP instrument was validated in the lab to perform at a 3-5 % radiometric and 0.5 % *DoLP* uncertainty across all spectral bands, though the HARP CubeSat and HARP2 may further reduce this uncertainty with improvements to on-board calibration and optical design (McBride et al. 2020, in prep). The study in this paper uses 3 % radiometric uncertainty for all the bands and 0.5 % *DoLP* uncertainty for 440 nm, 550 nm, and 670 nm as inputs to GRASP. The 870 nm polarimetric data is also used in the GRASP retrievals but due to lower signal-to-noise ratio in the field data compared to 440 nm, 550 nm, and 670 nm, we

145 give these data less relative weight in the retrievals. The total radiance (*I*) and *DoLP* are both useful for accuracy assessments and retrievals: they are not sensitive to reference plane that defines electric field $\vec{\mathbf{E}}$. *Q* and *U* as measured by AirHARP, on the other hand, are defined based on a reference plane and their absolute values depend directly on this chosen frame of reference. The details of this reference plane, including instrument scattering geometry, are described in the next section.

2.3 Definition of scattering geometry

150 Figure 2 defines the scattering geometry. Scattering angle (θ_{sca}) is defined as the angle between the sun vector and the viewing direction. θ_s is the solar zenith angle, θ_v is the instrument viewing zenith angle, ϕ_{sat} is the satellite azimuthal angle and ϕ_{sun} is the solar azimuthal angle. The relative azimuthal angle is $\phi = \phi_{sun} - \phi_{sat}$. For the calculation of $\theta_{sca,}$ we need to know θ_s, θ_v and ϕ.

The reference plane for the definition of $\mathbf{E}_\perp$ and $\mathbf{E}_\parallel$ is based on the local meridional plane, which is a standard reference frame

155 used for reporting Q and U (Emde et al., 2015). For detailed information please refer to the coordinate system as defined in the book by Hovenier et al. (2004). Q and U measured by AirHARP are based on the instrument reference frame and these are rotated to the local meridian plane that is formed of the local nadir vector plus the viewing zenith vector (see Fig. 2). The electric field parallel to the local meridian plane is called $\mathbf{E}_\parallel$ and the electric field perpendicular to the local meridian plane is $\mathbf{E}_\perp$. Using the information from aircraft Inertial Measurement Unit (IMU), the Q and U are rotated to the local meridional

160 plane from the instrument reference frame.

2.4 Aerosol Characterization from Polarimeter and LiDAR (ACEPOL)

The ACEPOL campaign was a collaborative effort of NASA and SRON (Netherlands Institute of Space Research) based out of Armstrong Flight Research Center (AFRC) in Palmdale, California, USA. One primary aim of the campaign was to acquire

165 data using airborne advanced passive and active remote sensing instruments, and then use the expanded information content available from the new sensors, both individually and in synergy, to better characterize aerosol (Knobelspiesse et al., 2020). Multiple polarimeters and lidars were mounted on the NASA ER-2 aircraft. These included AirHARP, as well as AirMSPI (Diner et al., 2013), RSP (Cairns et al., 1999, 2003), airborne SPEX (Smit et al., 2019), HSRL2 (Burton et al., 2018; Hair et al., 2008) and Cloud Physics Lidar (CPL) (McGill et al., 2002). ACEPOL also made use of ground-based instruments such as

170 AERONET and Micro-Pulse Lidar Network (MPLNET) for validation of aircraft measurements (Holben et al., 2001; Welton et al., 2001). The measurements and inversion algorithms used to analyze the ACEPOL data will be helpful in understanding the potential use of polarimeters in future satellite missions like the NASA PACE mission, the Aerosols, Clouds, Convection and Precipitation (A-CCP) Decadal Survey mission, and the European EarthCare mission. The ACEPOL campaign had nine flights over the period of October 19, 2017, to November 9, 2017, with a combined flight time of approximately 41.3 hours.

175 The main objectives of ACEPOL include the calibration of instruments over ocean and land with no clouds or aerosol, geolocation of image using coastlines, coordinated Cloud-Aerosol Lidar and Infrared Pathfinder Satellite Observation (CALIPSO) or Cloud-Aerosol Transport System (CATS) under flights, validation with AERONET in low, medium and high aerosol loading, satellite intercomparison for aerosol and cloud retrievals, and calibration over a spatially uniform surfaces amongst other lower priority goals, such as cirrus cloud observations. (Knobelspiesse et al., 2020)

180 For the ACEPOL 2017 campaign, the AirHARP instrument was mounted on an ER-2 aircraft left wing pod. It collected data over 8 flights consisting of a total of 45 flight leg images. For this study, we have analyzed only eleven of these flight legs,

listed in Table 2, including scenes over the ocean, dry lakes, forest fire smoke, and AERONET sites. Along with the airborne polarimeters, the HSRL2 also flew aboard on the ER-2 aircraft during ACEPOL. HSRL-2 is a NASA high spectral lidar that has been used to measure clouds and aerosols (Burton et al., 2012; Hair et al., 2008). HSRL2 measures extinction coefficients

185 at two wavelengths (2α at 355 and 532 nm) and backscattering coefficients at three wavelengths (3β at 355, 532 and 1064 nm) (Burton et al., 2018). These measurements allow the detection of the vertical distribution of aerosol extinction with a precision of about 0.02 km^{-1}. The HSRL2 instrument points at nadir and measures the vertical profile of aerosol backscatter coefficient at 0.1Hz frequency with a vertical resolution of 15m and aerosol extinction coefficient at 1 minute temporal resolution and 150 m vertical resolution.

190 3 Aerosol retrievals from AirHARP using GRASP

3.1 Atmospheric gas absorption correction for aerosol retrieval

Before the inversion of the AirHARP measured I, Q and U components, each measured pixel must be prepared for aerosol retrievals. This involves first avoiding groups of pixels that are inappropriate for an aerosol retrieval, such as clouds, and correcting for gaseous absorption in the remaining signal. Automatic algorithm-level cloud masking can be challenging. In the

195 work presented here, scenes were selected by eye, so that there was no need to develop an automatic cloud mask for AirHARP at this time. However, correction for gaseous absorption was necessary. I, Q, and U are corrected for the atmospheric gas absorption using the technique mentioned in Patadia et al. (2018). For AirHARP spectral bands, gas absorption is most significant at the 550 nm and 670 nm bands and is mainly due to the four atmospheric gasses O_2, H_2O, O_3, and NO_2. Columnar optical depth of 0.004, 0.032, 0.014, and 0.003 due to atmospheric gases are observed at 440 nm, 550 nm, 670 nm and 870 nm

200 spectral bands respectively. The radiative transfer model: Unified Linearized Vector Radiative Transfer Model (UNL-VRTM) (Wang et al., 2014; Xu and Wang, 2019) is used to calculate transmission due to the total effect of all atmospheric gas absorption, which is translated to a multiplicative correction factor for each of the four AirHARP bands. These correction factors are a function of the path length through the atmosphere, which is a combination of solar and instrument viewing zenith. All the calculations are done for a mid-latitude summer US atmosphere assuming no variation in the four gases and for an

205 AirHARP observation height of 20 km above sea level. This correction is applied to each band, for each pixel, prior to the inversion.

3.2 Generalized Retrieval of Aerosol and Surface Properties (GRASP)

GRASP is a versatile retrieval algorithm that can be used for a variety of remote sensing and in-situ measurements to retrieve aerosol and surface properties (Dubovik et al., 2014). It is open-source software and is available free to non-commercial users

210 for downloading from the website https://www.grasp-open.com/. GRASP first demonstrated its overall capability in an aerosol retrieval test study (Kokhanovsky et al., 2015). It has gone on to prove itself in a variety of real-world applications (Chen et al., 2018, 2019; Frouin et al., 2019; Li et al., 2019; Schuster et al., 2019; Torres et al., 2017). GRASP has been successfully

applied to measurements from many different types of instruments (Benavent-Oltra et al., 2019; Espinosa et al., 2017, 2018; Román et al., 2018; Titos et al., 2019; Torres et al., 2017), but the most pertinent to AirHARP are the previous applications of

215   GRASP to POLDER-3 on PARASOL (Chen et al., 2018, 2019; Dubovik et al., 2011; Frouin et al., 2019; Li et al., 2019) because of its familiar polarization, multi-wavelength, and multi-angle sampling characteristics.

GRASP consists of two modules: a forward model and an inversion module. For the case of aerosol measurements, the forward model consists of a polarized Radiative Transfer (RT) code to calculate the radiance measured by the instrument and it also consists of a kernel to calculate the contribution of single scattering by the aerosol particles. For the RT calculations, GRASP

220   uses a Successive Order of Scattering (SOS) scheme. The RT module consists of different surface Bi-Directional Reflectance Distribution Function (BRDF) and Bi-Directional Polarized Distribution Function (BPDF) models for land and ocean. These models are briefly discussed in Appendix A, and further information about the RT code and single scattering database that are beyond the scope of this paper can be found in (Dubovik et al., 2011; Lenoble et al., 2007). The single-scattering kernel that we employ for the AirHARP retrieval uses five fixed log-normal distribution modes as described in Table 3. Each of those

225   modes has a fixed mode radius and width. The only free parameter in the retrieval for particle size distribution is the concentration of particles in each bin. There are three lognormal modes in the fine mode and two in the coarse mode.

The inversion module in GRASP uses the multi-term least square method (LSM) to solve the following system of equations,

$$\mathbf{f}^* = \mathbf{f(a)} + \triangle_{\mathbf{f}} \qquad\qquad 3.1$$
$$\mathbf{0}^* = \mathbf{Ga} + \triangle_{\mathbf{g}}$$
$$\mathbf{a}^* = \mathbf{a} + \triangle_{\mathbf{a}}$$

where a is a vector of unknowns and is called a *state vector*. $\mathbf{f}^*$ is the vector which contains the instrument observations, $\triangle_{\mathbf{f}}$ is the uncertainty in the observations, and $\mathbf{f(a)}$ is the forward model simulated observations. For the AirHARP observations,

230   $\mathbf{f}^*$ is a vector containing information of *I*, *Q/I*, and *U/I* or *I* and *DoLP* for all the spectral bands and viewing angles. Given an ideal pixel, AirHARP measures 120 data points for each aforementioned variable. A priori smoothness constraints are imposed on the retrieved solution in order to suppress unrealistic oscillations in the retrieved characteristics. The second equation in Eq. 3.1 represents such smoothness constraint on the retrieved characteristics, $\mathbf{0}^*$ is the zero vector and it imposes the forced constraint that the derivatives of retrieved parameters to be zero. The matrix $\mathbf{G}$ includes the coefficients for calculating

235   derivatives of state vectors approximated by finite differences. For example, unrealistic oscillations in particle size distribution are eliminated using coefficients calculated from derivatives with respect to radius. Similarly, spectral dependencies of refractive index are imposed using the coefficients calculated using wavelength. Uncertainties in the smoothness constraints are represented by the $\triangle_{\mathbf{g}}$ term. For the AirHARP retrievals, we use the predetermined five-modal log-normal distribution mentioned in Table 3, unless otherwise stated. The volume median radius and standard deviation for each mode are fixed and

240   only the particle volume concentration is allowed to vary. Also, we use a priori constraints on the particle size distribution and these constraints are represented by third and last term in Eq. 3.2. A priori estimates of state vector parameters are given by $\mathbf{a}^*$ and $\triangle_{\mathbf{a}}$ is the uncertainity in the a priori constraints of a^*. The multi term LSM in GRASP finds the statistically optimized solution of the set of equations mentioned in Eq. 3.1 by minimizing the term,

$$2\Psi(\mathbf{a}) = (\mathbf{f(a)} - \mathbf{f}^*)^T \mathbf{W_f^{-1}}(\mathbf{f(a)} - \mathbf{f}^*) + \gamma_g \mathbf{a^T W_g^{-1} G a} + \gamma_a (\mathbf{a} - \mathbf{a}^*)^T \mathbf{W_a^{-1}}(\mathbf{a} - \mathbf{a}^*) \qquad 3.2$$

where, $\mathbf{W_f} = \frac{1}{\epsilon_f^2}\mathbf{C_f}$ is the weighting matrix calculated using the measurement covariance matrix $\mathbf{C_f}$ and the first diagonal

245 element ϵ_f, in the $\mathbf{C_f}$. Similarly, $\mathbf{W_g} = \frac{1}{\epsilon_g^2}\mathbf{C_g}$, $\mathbf{W_a} = \frac{1}{\epsilon_a^2}\mathbf{C_a}$, are calculated using the covariance matrices of a priori smoothness

constraints and a priori constraints on the of the retrieved parameters. $\gamma_g = \frac{\epsilon_f^2}{\epsilon_g^2}$, and $\gamma_a = \frac{\epsilon_f^2}{\epsilon_a^2}$ are the *Lagrange multipliers*

(Phillips, 1962; Tikhonov, 1963) calculated using the information from the covariance matrices. Since we assume that all the

input variables have log-normal error distribution, the solutions to the set of equations in Eq. 3.1 are found by minimizing the

term $\Psi(\mathbf{a})$ in Eq. 3.2 using the Levenberg-Marquardt iterative method. For more detailed information on the theoretical

250 background of the GRASP retrievals, please refer (Dubovik, 2006; Dubovik et al., 2011; Dubovik and King, 2000).

The state vector *a* includes the information on particle size distribution which is the concentration for five log-normal modes

of Table 3, the complex refractive index in the four spectral bands that are independent of particle size, the fraction of spherical

particles (SF), aerosol layer height, and parameters characterizing the directional reflectance of the surface. AOD is derived

from retrieved aerosol properties using the method mentioned in appendix B.1. Additionally, fine mode AOD is calculated

255 using modes 1-3 mentioned in Table 3 and coarse mode AOD using modes 4 and 5. Single Scattering Albedo (SSA), Angstrom

Exponent (AE) are also derived from the retrieved aerosol properties. Even though aerosol layer height is retrieved during the

retrieval process, the sensitivity to aerosol height for the AirHARP wavelengths is negligible for most of the low loading cases.

Retrieved aerosol layer height is thus not discussed in this work. In the next section, we discuss the results of applying GRASP

to AirHARP measurements of *I*, *Q* and *U* for selected cases from the ACEPOL campaign.

260 4 Aerosol properties from AirHARP measurements

4.1 Selected cases from ACEPOL 2017

We will focus on four specific cases from ACEPOL 2017 to illustrate the measurement characteristics of AirHARP and

demonstrate the GRASP retrieval. Figure 3 shows color composite imagery of the intensity and DoLP of each case, using the

440, 550 and 670 nm bands. Cases include a scene over the ocean with little aerosol loading (23 October 2017; T21:30 UTC),

265 a scene over Rosamond Dry Lake (25 October 2017; T18:26 UTC), and two scenes of forest fire smoke (27 October 2017;

18:16 UTC and 9 November 2017; 19:30 UTC).

4.2 Scene over the ocean (23 October 2017 T21:30 UTC)

The first of our analysis scenes is a cloud-free segment where the ER-2 flew over the USC SeaPRISM AERONET station

located at 33.564N, 118.118W, on a platform off the coast of southern California. The AERONET station measured a low

270 aerosol loading of AOD = 0.04 at 440 nm at the time of ER-2 overpass. The segment includes sun glint, and because of the

low AOD, the sun glint and non-sun glint pattern are ideal for the intercomparison of different polarimeter measurements of *I*,

Q, *U*, and *DoLP*. This flight track aligned with the solar principal plane so that the longer wavelength bands will be highly polarized for the sunglint viewing angles. For a scene with low aerosol loading above the ocean with no sun glint, the polarization follows the Rayleigh pattern and will peak at the 90-degree scattering angle. For the sunglint case, we expect the

275   peak to be at scattering angles where the sunglint is observed. In this case, the maximum sun glint occurs for scattering angles 70º to 90º. Figure 4 shows the measured *I*, *Q/I*, *U/I* and *DoLP* for one pixel (footprint of 55 m x 55 m) along the nadir track as a function of scattering and plotted as colored circles, for each of the four wavelengths. The measurements show that the maximum intensity occurs in the glint region (scattering angles 70º to 90º) and confirms that the *DoLP* peak also occurs at the sunglint scattering angles. However, while the intensity falls to minimum levels outside of the glint region, the *DoLP* has a

280   more gradual fall off, as the Rayleigh pattern with maximum DoLP at 90º is superimposed on the dark ocean scene.

GRASP is applied to invert the measured *I*, *Q/I* and *U/I* for the pixel represented in Fig. 4 for aerosol retrievals. The ocean surface model used is the NASA GISS model (Mishchenko and Travis, 1997) based on Cox and Munk (1954), in which the ocean surface reflectance is represented by three parameters: ocean surface albedo, the fraction of Fresnel reflection surface,

285   and wind speed denoted by a_0, a_1, and a_2 respectively, with details given in Appendix A.2. Because the aerosol loading is very low for this scene, there is insufficient aerosol loading to retrieve the real (RRI) and the imaginary (IRI) part of the complex refractive index, and instead are constrained (RRI = 1.4 and IRI = 0.0001) in GRASP using an oceanic aerosol model mentioned in Hasekamp et al. (2008). The five-mode particle size distribution (Table 3) is used in the retrieval, with the concentrations of each of the five modes unconstrained. Therefore, the retrieved parameters include the five concentrations for

290   the five lognormal modes shown in Table 3, aerosol spherical fraction, aerosol layer height, and the ocean model parameters a_0, a_1, and a_2. AOD is derived from the retrieved and modeled parameters. The solid black lines plotted in all panels of Fig. 4 are the GRASP fits using the AirHARP measured *I*, *Q/I*, and *U/I* as input. The *DoLP* is also calculated from the fitted variables and plotted in the same figure. The sunglint registers in *I* as a sharp peak with the width of that peak dependent on surface roughness primarily caused by surface wind. The retrieval of aerosol properties is highly sensitive to wind speed. An

295   inappropriate wind speed estimate can result in high uncertainty in the aerosol properties retrieved. The goodness of the fit in Fig. 4 suggests that retrieval of the ocean parameters, including wind speed is very good for this sampled pixel.

To achieve a better understanding of how well the GRASP retrieval can fit the measurements, we apply the retrieval to 3600 pixels (60 x 60) of this ocean scene. Here, a pixel footprint of 55 m x 55 m is used, since the variability due to the geolocation is negligible for an open ocean pixel as compared to a land pixel. Figure 5 shows two-dimensional density scatter plots of the

300   AirHARP measured variables, *I*, *Q/I*, and *U/I* for the four spectral bands, versus the GRASP fit, and the histogram of the number of points used for each bin is plotted on the respective axes. A dashed magenta line represents the Ordinary Least Square (OLS) fit between retrieved and measured parameters, a black solid line denotes the 1:1 line. The goodness of fit, χ^2_{norm} for each pixel, is calculated using the mathematical expression mentioned in Table 4. A list of the statistical parameters

305   used in this study are formulated in Table 4, where x_i is the measured value, and y_i is the GRASP fit. *N* is the total number of

observations for the pixel, $\mathbf{S_y}$ is the error covariance matrix for the observations. $\mathbf{S_y}$ includes only diagonal elements and off-diagonal are assumed to be zero since we do not consider the cross-correlation between the different viewing angles for the same spectral band. For the reduced radiance I, all spectral bands show a good comparison at lower I values, within the χ^2_{norm} confidence interval, and show a slight deviation from the 1:1 line for the sunglint angle data points. The GRASP fit in blue

310   band yields an underestimated I when its values are greater than 0.2, giving an overall OLS slope of 0.967. However, the range where the underestimation occurs represents only a small fraction of the total analyzed samples. This underestimation is also observed for the 550 nm band with a slightly better R^2 value of 0.995 compared to 0.986 for the 440 nm band. For the case of 670 and 870 nm bands, we observed a slight overestimation with the GRASP fitting having R^2 values 0.997 and 0.996 for red and NIR bands respectively. Some of this under and overestimation is because the isotropic wind model has trouble simulating

315   the multi-angle views in the sun glint region. In terms of the spread of points around the regression line, we expected much higher noise for the 870 nm band due to the lower signal to noise ratio (SNR) in this band. Surprisingly, in terms of fitting the I component, the 870 nm band does not display any repercussion of the lower SNR. For the polarization components Q/I and U/I, all the spectral bands demonstrate a good correlation between the GRASP fit and AirHARP measurements. This clearly demonstrates that the polarization variables are less affected by the discrepancies in sunglint pixels for the extreme viewing

320   angles. The average AOD retrieved for these 60 pixels by 60 pixels region are 0.07±0.03, 0.04±0.02, 0.03±0.01, and 0.02±0.01 at 440 nm, 550 nm, 670 nm, and 870 nm respectively. In the following section, we detail several case studies of AirHARP land surface, and aerosol plume data applied to GRASP for retrieval of aerosol microphysical and optical properties.

4.3 GRASP retrieval over land

For the GRASP retrieval applied to measurements over land, the Ross-Thick Li-Sparse BRDF model is used to represent the

325   directional reflectance from the surface, which uses three parameters K_0, K_1, K_2. K_0 is a spectrally dependent parameter that represents the isotropic reflectance, K_1 and K_2 normalized to K_0 are the spectrally independent parameters which are the coefficient of geometric and volumetric scattering kernels respectively (Maignan et al., 2004; Wanner et al., 1995). Polarized reflectance from the surface is modeled using the Maignan-Breon one-parameter model and the retrieved parameter is a scaling factor that is spectrally dependent (Maignan et al., 2009). Refer to Appendix A.1.3 for detailed information on the surface

330   models. Equally important over the land for a multi-angle instrument is the need to co-register each along-track view angle of the same target. Over the flat ocean, co-registration is straightforward and is based on a projection of the measurements onto a representation of a smooth geoid Earth. Over the land, topography introduces a challenging situation in which forward and aft views of the same target might image different slopes of a ridge. Topographically corrected projections need to be made either to a digital elevation model at a resolution comparable to the measurements (this is operational for AirHARP Level 1B

335   data), or the measurements need to be projected to a specific altitude in the atmosphere, perhaps cloud top height or to an aerosol layer. Figure 6 shows the measured I, Q/I, U/I and $DoLP$ from the 550 nm wavelength for selected pixels in each of the following three flight legs under analysis. In this figure, unlike Fig. 3, the ocean scene is from an offglint pixel. The other pixels represent a dry lake surface, vegetation, and smoke, respectively. Also plotted as the black curves are the GRASP fit to

each of these targets. The ocean pixel appears the easiest to fit, and then the smooth dry lake pixels. The other land surface

340   types, with their variable topography, present a greater challenge for GRASP. In the next section, we detail these three flight

segments over land that include, one on 25th October 2017 over Rosamond dry lake at 18:16 UTC, a second one that is a forest

fire smoke scene near the Kaibab National Forest and Grand Canyon National Park in Arizona, USA on 27th October 2017 at

18:16 UTC, and a third scene of fresh smoke on 9th November 2017 at 19:30 UTC.

4.3.1 Rosamond dry lake and surrounding vegetation (25 October 2017 T18:26 UTC)

345   The flight leg with Rosamond dry lake on 25 October 2017 T18:26 UTC, is a scene with very low aerosol loading according

to the Moderate Resolution Imaging Spectroradiometer (MODIS) retrieval of AOD at 550 nm = 0.03. The minimal AOD

allows for the measured signal to be dominated by surface reflectance features. The retrieved AOD of the pixel of the dry lake

whose measurements and GRASP fit are shown in Fig. 6(b) were 0.05, 0.04, 0.04, 0.04 for the 440 nm, 550 nm, 670 nm, and

870 nm bands, respectively. Measurement and GRASP fit for another pixel from the same scene but over nearby vegetation

350   (farm field) is plotted in Fig. 6(c) and the retrieved AOD are 0.04, 0.03, 0.03, 0.02 for 440 nm, 550 nm, 670 nm, and 870 nm

bands respectively. Note that GRASP retrieves a very similar atmosphere over both surfaces. Yet, in Fig. 6(b) the homogenous

surface of the dry lake provides a simpler retrieval and the result is a better fit to the measurements than does the more complex

surface presented by the vegetation. The RGB image of the flight leg on 25 October 2017 at 18:26 UTC is plotted in Fig. 3(b).

4.3.2 Forest fire smoke (27 October 2017 T18:16 UTC)

355   Up to now, all our examples have demonstrated AirHARP measurements and GRASP retrievals in very low aerosol loading.

These situations can demonstrate GRASP ability to fit the measurements and to return values for spectral AOD. The low

aerosol loading does not supply enough signal to fully characterize the aerosol using GRASP. The final example that we show,

the flight leg on 27 October 2017 at 18:16 UTC, captures a fire and smoke plume with significant aerosol loading. This will

demonstrate the potency of AirHARP/GRASP to characterize aerosol particle properties, along with loading. This case has

360   complicated terrain and due to the higher resolution of the pixels, the aerosol retrievals from this scene will be complicated.

As a quick check, we show the GRASP retrieval fit to the input measurements in Fig. 6(d) for a single pixel in the smoke

plume where the terrain is not that complicated and homogenous smoke is observed. The retrieval is fitting to the measurements

well. AOD retrieved at this pixel is 1.62, 1.2, 0.85 and 0.51 for the 440 nm, 550 nm, 670 nm, and 870 nm bands, respectively.

An RGB image of the smoke scene on 27 October 2017 at 18:16 UTC is plotted in Fig. 7 with X and Y axis as pixel locations.

365   The GRASP algorithm is applied to 7150 pixels in a large area marked by the red rectangle as shown in Fig. 7, and retrievals

for the whole segment are plotted in Fig. 8. Retrievals include AOD, RRI, IRI, and SSA at the four spectral bands of AirHARP.

AOD is plotted across the image, but the intrinsic particle properties are only shown where GRASP recognizes enough aerosol

loading to be sensitive to particle properties. Thus, the plots follow the smoke plume. For the retrievals, a combination of Ross-

Li and Maignan-Breon land surface BRDF and BPDF models are used to represent the directional reflectance from the land

370   surface. The pixels are spatially averaged to a resolution of 550 m x 550 m to avoid the micro pixel movement effects which

will affect the aerosol retrievals. High non-homogenous smoke near the source makes accurate aerosol retrieval difficult. This is because the GRASP assumes a plane parallel aerosol layer in the radiative transfer multi-angle calculations, whereas in reality at different viewing angles we are seeing different locations in the plume, which introduces complications in the radiative transfer calculations.

375 Figure 8 (a) shows the retrieved AOD for the 440 nm, 550 nm, 670 nm, and 870 nm spectral bands. The AOD at 440 nm band is much higher than the one at 870 nm band as we expect for the fine forest fire particles. For the higher confidence in the retrieved results, pixels with $\chi^2_{norm} > 5$ and $AOD_{440\ nm} < 0.4$ are removed from the analysis of SSA, RRI, IRI, AE, aerosol volume concentration, and SF. Retrieved forest fire smoke optical properties from the flight leg on 27 October 2017 at 18:16 UTC using AirHARP observations are close to values seen previously in the literature. The values of RRI retrieved from

380 AirHARP and shown in Figure 8(c) can be represented as a Gaussian distribution with a mode value of 1.55 for all wavelengths, while retrievals from the RSP instrument during the ACEPOL campaign produced values of RRI of 1.56 (Fu et al., 2020). Fire Laboratory at Missoula Experiments (FLAME) records the real part of the refractive index in a range from 1.55 to 1.8, depending on the composition of the smoke particles (Poudel et al., 2017). FLAME 2 laboratory experiments reported RRI values in the range 1.54 to 1.67 depending on the fuel source (Mack et al., 2010). The AirHARP retrievals of IRI range from

385 0.01 to 0.1 with a mean value of 0.024 (Figure 8(d)), which compares well with the FLAME database range of 0.01 to 0.5 and FLAME 2 database range of 0.011 to 0.217 (Mack et al., 2010). Another smoke optical property study reports SSA in the range of 0.78 to 0.94 at 532nm, depending on the age of the smoke (Nicolae et al., 2013). Our retrieved SSA from AirHARP in this work (see Fig. 8(b)) ranges from 0.6 to 0.99 with a mean value of 0.87±0.06, 0.86±0.07, 0.84±0.08, and 0.81±0.09 for 440nm, 550nm, 670nm, and 870nm, respectively. Retrieved single scattering albedo values are well within the range measured

390 during the FLAME 2 experiment using a photo acoustic spectrometer and a nephelometer. Fine and coarse mode AOD calculated using the log-normal modes listed in the Table 3 are plotted in Fig. 9(a) and 9(b). The main contribution to AOD is from the fine particles (log-normal modes 1 to 3 in Table 3) with almost no contribution from coarse mode (log-normal modes 4 and 5 in Table 3). The retrieved volume median radius for the fine mode ($r_{v,fine}$ (see Eq. B.1.6)) is 0.157±0.024 μm with $\sigma_{v,fine} = 0.550\pm0.026$ μm. Figure 10(a) shows the AE derived for each pixel calculated using 440nm and 870nm spectral bands.

395 Figure 10(b) and 10(c) are aerosol volume concentration ($\mu m^3 \mu m^{-2}$) and SF retrieved respectively for each pixel inside the red box in Fig. 7. The Angstrom exponent retrieved from our measurement has a mean value of 1.53 with a standard deviation of 0.336. Also, we see a significant number of pixels with AE >2 which is considered to be fresh smoke (Nicolae et al., 2013). In the smoke scene retrieved from AirHARP measurements the mean value of the percentage of spherical particles is 50 % with a standard deviation of 36 %. It essentially means that the retrieved particle shape of the smoke particles have been

400 retrieved as highly non-spherical for much of the smoke plume, while reports from SPEX and RSP for the same smoke scene indicate the opposite with 99 % and 85 % spherical for SPEX and RSP, respectively (Fu et al., 2020). However, we see that in our retrievals for the scene in Fig. 7 there are significant number of smoke pixels with spherical fraction close to 100 % (see Fig. 10(c)). While smoke properties are often spherical (Manfred et al., 2018; Martins et al., 1998), non-spherical fractal shapes can be seen in scanning electron microscopy (Chakrabarty et al., 2006). There is no definite answer whether the results shown

405 in Fig. 10(c) are a retrieval artefact or are physically true. We do know from experimentation that the GRASP retrievals in this situation was not particularly sensitive to particle shape, returning the same values for AOD and SSA, within uncertainty bounds, whether SF was held constant at 80-99 % or whether it was a free parameter and retrieved as in Fig. 10(c). A table of retrieved and derived parameters is listed in Table 5. In order to check the quality of the data fitting for the smoke scene of Fig. 7, 8, 9 and 10, 2D density plots of measured and fitted variables, I and $DoLP$, for all spectral bands are plotted in Fig. 11.

410 Figures 11 (a), (c), (e) and (g) show the 2D density plot for the reduced radiance I measured at four spectral bands 440 nm, 550 nm, 670 nm, and 870 nm respectively. 2D density plot of the measured and GRASP fitted $DoLP$ at 440 nm, 550 nm, 670 nm, and 870 nm are plotted in the Fig. 11(b), (d), (f) and (h) respectively. The fit for $DoLP$ in 870 nm band has a higher spread in the density plot compared to the other spectral bands because the Silicon-based detector used for imaging in AirHARP has a lower quantum efficiency at 870 nm compared to the three other wavelengths. 550 nm and 670 nm bands data shows the best

415 correlation to GRASP fit with $R^2 = 0.991$ and 0.993 for I, whereas, 440 nm and 870 nm have $R^2 = 0.986$ and 0.990 respectively. Ordinary Least Square (OLS) regression for the 440 nm yields a slope of 0.984, which is the least performing band for the variable I, followed by 870 nm, 550 nm, and 670 nm spectral bands. For the case of $DoLP$, 870 nm has the lowest R^2 value of 0.960, followed by 670 nm ($R^2 = 0.991$). Both 440 nm and 550 nm bands have an R^2 value of 0.995. Unlike the variable I, the $DoLP$ in the 550 nm band shows more deviation from the 1:1 line with a slope of 0.964 for OLS regression fit. Overall, the

420 2D density plots reveal that the fitting for each variable I and $DoLP$ generated using the GRASP and AirHARP measurements performs well for the smoke scene in Fig. 7. Since the retrieval is an ill-posed mathematical problem, we need to make sure that the retrieved values are reasonable and compatible with co-incident instruments. For the case of the ACEPOL campaign, AOD from the AirHARP-GRASP retrievals are verified by comparing it with HSRL2 and AERONET observations. In the next subsection, we use the flight leg on 9th November 2017 at 19:30 UTC to compare the AOD retrievals from AirHARP with

425 the collocated HSRL2 measurements.

5 Comparison of AirHARP GRASP retrievals with collocated data sets

5.1 High Spectral Resolution LIDAR-2 (HSRL2) vs AirHARP AOD comparison

HSRL2, flying on the same aircraft with AirHARP during ACEPOL provides the opportunity to compare the GRASP retrievals of AOD with an independent and collocated measurement. AirHARP lacks a wavelength channel identical to the wavelengths

430 measured by HSRL2; therefore, for this study, we make use of the 440 nm and 550 nm channels on AirHARP to calculate the Angstrom exponent and then use that information to interpolate the AOD to HSRL2's wavelength of 532 nm. We collocate HSRL2 and AirHARP measures of AOD for the smoke plume shown in Fig. 3(d), (9 November 2017; 19:30 UTC). The smoke plume in this image is a controlled fire started in the Kaibab National Forest, Arizona, USA and is highly non-homogenous near the source fire. To match the HSRL2 ground pixel in the AirHARP image, the latitude and the longitude are matched to

435 a tolerance level of about 200m on the ground. For this flight leg, HSRL2 reports the aerosol extinction at 10 s intervals, which translates to 2 km in the ground distance for an ER-2 aircraft flying at 20 km altitude with a speed of ~200 m/s, but with a

narrow cross-track footprint of only 15 m. Thus the 2000 m x 15 m footprint of the HSRL2 measurements are inherently mismatched with AirHARP's 275 m x 275 m pixels. Given the inhomogeneity of this aerosol, we do not expect perfect agreement between the two sensors' retrieved AODs, simply because of the mismatch in spatial sampling.

440   For this study, we make use of the HSRL2 AOD at 532 nm, where an assumption of the lidar ratio is not required. All the GRASP retrievals for this comparison are done using the *I* and *DoLP* measurements from AirHARP. Aerosol optical depth at 532 nm as a function of the collocated along-track pixels is plotted in Fig. 12(a), and the scatter plot of the comparison is shown in Fig. 12(b). In Fig. 12(a) HSRL2 measured AOD is denoted by the green diamond markers, and AirHARP AOD the grey squares. Each square represents the mean of 28 pixels around the collocated HSRL2 ground pixel in the AirHARP image.

445   We used 7 pixels along-track (~1.93km) and 4 pixels cross-track (~1.1km) to find those mean values. The error bar in the AirHARP data points is the standard deviation of AOD of all pixels within the ~1.93 km x 1.1 km region around the HSRL2 ground pixel, representing the spatial variability of the smoke plume within the averaging rectangular box. For this heterogenous smoke plume case, we had to apply $\chi^2_{norm} < 20$, to filter out bad pixels/fits. Non-homogeneity of the smoke makes the retrieval complicated since we see different parts of the smoke plume when we scan through the different viewing

450   angles of AirHARP data. So, using a higher χ^2_{norm} value for filtration helps to catch the higher AOD values. A scatterplot of these two data sets is shown in Fig. 12(b) and the solid black line is the 1:1 line whereas, the yellow error bar represents the spatial variability of AirHARP AOD similar to that in Fig. 12(a). A comparison of HSRL2 measured AOD at 532 nm with the AirHARP AOD retrievals at 532 nm shows a strong, positive correlation and only deviates when the plume is thick and heterogeneous. A Pearson correlation coefficient (ρ) of 0.940, *BIAS* = -0.062, and Mean Absolute Error (*MAE*) = 0.122 is

455   obtained for this comparison. Matching the HSRL2 AOD in regions of heterogeneity is challenging using 1D plane-parallel aerosol assumptions; the aerosol layer must be characterized first, i.e. from the HSRL2 AOD vertical profile, and used as input in a 3D radiative transfer simulation to calculate *I*, *Q* and *U* for the scene at different viewing angles. Also, the different cross-track pixel size between the HSRL2 and AirHARP measurement makes the intercomparison difficult to interpret in some cases. For points near the plume source, higher pixel variability may also bias AirHARP AOD retrievals performed at the same

460   general location as the HSRL2 measurement.

5.2 AERONET vs AirHARP AOD comparison

Validation of AirHARP-GRASP retrievals using AERONET measured aerosol optical depth for the collocated AirHARP pixels during the ACEPOL campaign are discussed in this section. A list of the collocated AERONET stations and

465   measurements used for this analysis are listed in Table 2. For the AERONET validation, AirHARP pixels with a resolution of 550m x 550m are used for the GRASP retrievals to avoid the issues due to the small pixel shifting during the reprojection to a common latitude-longitude grid as well as to avoid strong fine resolution surface features that appear over the urban area. To further protect the algorithm from subpixel inhomogeneity and other features inappropriate for retrieval a $\chi^2_{norm} < 1.5$ filter is used to remove the bad pixels/fits which may be caused by the presence of thin clouds or due to the inability of surface

470   reflection models to represent the directional reflectance from a complicated surface. To collocate the AERONET pixel in the
        AirHARP image, the latitude and longitude of the AERONET location are matched to the AirHARP latitude and longitude
        with a tolerance of 2×10^{-3} degree, which is approximately equivalent to 200m on the ground. An area of 5.5 km x 5.5 km
        around this collocated pixel is used to calculate the area mean AOD from the AirHARP retrievals, and this is matched to a
        one-hour temporal mean from AERONET measurements. Each of the 5.5 km x 5.5 km averaging boxes includes 100 pixels,

475   however many of them are removed after the χ^2_{norm} filtering. Due to the low loading of aerosol over the AERONET stations,
        treating the aerosols as a mixture of predefined aerosol components with fixed size and shape distributions, and complex
        refractive index will benefit the accuracy of AOD retrievals using AirHARP and GRASP. A five-component mixture of the
        aerosol is used to create the phase matrix kernels, which includes the aerosol types: biomass burning, urban, urban polluted,
        maritime, and desert dust. Among these, only desert dust is considered as completely nonspherical and uses a shape distribution

480   mentioned in (Dubovik et al., 2006). All the other types are treated as 100 % spherical particles. The details of the bi-modal
        size distribution parameters along with the fixed complex refractive index for each of the aerosol types are tabulated in Table
        6 and are based on the work of Dubovik et al., 2002. Figure 13 shows the particle size distribution as a function of radii for the
        different aerosol types. The main differences between the five log-normal mode kernel-based retrievals are, 1.) instead of
        retrieving the concentration of each log-normal mode, weight for each of the aerosol components mentioned in the Table 6 are

485   retrieved. 2) RRI, IRI, and SF are not retrieved since these are fixed for each of the aerosol components. This simplified
        approach significantly drops the complexity of the aerosol model by reducing the number of parameters retrieved in the joint
        retrieval. It helps in reducing the nonlinearity of the inverse problem and makes the separation of the surface and aerosol signal
        much less complicated compared to a five-lognormal mode kernel. The maximum AOD measured by a collocated AERONET
        station during the ACEPOL campaign is 0.158 at 440 nm and using this simplified aerosol type model will greatly benefit the

490   AOD estimation from AirHARP GRASP retrievals. The Rahman-Pinty-Verstraete (RPV) BRDF surface model along with the
        Maignan-Breon BPDF models are used for representing the directional reflectance from the land surface. RPV BRDF model
        perform better over the urban and barren land area compared to Ross-Li BRDF kernels. AERONET measured AOD are
        interpolated to AirHARP spectral bands for 1:1 comparison. Figure 14 shows the scatterplot of these two data sets with
        $AOD_{AERONET}$ in the X-axis and $AOD_{AirHARP}$ on the Y-axis. The standard deviation of AOD within this 5.5 km x 5.5 km box is

495   indicated using the error bar in Fig. 14. Statistical parameters that represent the correlation between these two data sets are
        tabulated in the table inside Fig. 14. The black dashed lines in Fig. 14 are AOD(1:1) $\pm$ 0.04 lines. Mean absolute error of 0.014,
        0.013, 0.013 and 0.017 are obtained for the spectral bands 440, 550, 670 and 870 nm respectively, with 870 nm band having
        slightly higher spread than the other bands. Also, a similar trend is seen for 870 nm in the case of BIAS, where 440, 550, and
        670 nm band have a BIAS of -0.011, -0.013, 0.011 respectively whereas 870 nm has a BIAS of -0.017. At low AOD we can

500   see a low bias compared to AERONET AOD measurements, which is similar to what we see for RSP vs AERONET
        comparison in (Fu et al., 2020). Overall, the performance of the AirHARP observations plus the GRASP retrieval algorithm
        gives a good correlation with the collocated AERONET observations.

6 Future research

505   We note the abundance of very low aerosol loading in the majority of the ACEPOL flight legs. Future work should make use of these data to focus on surface characterization using the AirHARP/GRASP combination. There are several flight segments over the Rosamond Dry Lake, in California, USA in different flight directions and because the dry lake is relatively flat and uniform, it becomes an ideal target for testing GRASP retrievals of surface BRDF and BPDF parameters. Furthermore, on this day, at AirHARP overpass, ground measurements of radiance and polarized radiance were made using the Ground Multiangle Spectro-Polarimetric Imager. This will be a perfect case for a case study on the performance of different BRDF + BPDF kernel

510   combinations to represent the directional reflectance from a bright surface. This data set can be used to improve the BRDF/BPDF model at an unprecedented higher resolution compared to previous studies (Maignan et al., 2004, 2009). This will help in better characterization of directional reflectance from the urban surface and will benefit the overall accuracy of AOD retrievals over the land.

7 Conclusions

515   In this study, AirHARP polarimetric measurements, taken at the high angular and spatial resolution over a wide swath, combined with the GRASP algorithm allow for unprecedented spatial mapping of aerosol properties that are consistent with co-incident instrument retrievals. These properties always include AOD, but can also deliver real and imaginary parts of the refractive index, particle size information, spherical fraction, and single scattering albedo when aerosol loading is sufficiently high. We demonstrated that the measurements match the forward model calculations in a variety of environments: the retrieval

520   performs well over barren land surface and vegetation, though retrievals over sunglint still show biases in the AOD. The wide swath of the AirHARP enables the aerosol retrievals over a large scene of interest, which makes the AirHARP instrument unique from many of the other airborne polarimeters available as of today. Also, this wide swath will help in capturing more aerosol events globally compared to a narrow swath multi-angle polarimeter, when the HARP concept is applied to space sensors.

525

In situations with low aerosol loading (AOD < 0.17) over land, AOD retrieved from AirHARP using GRASP, matches collocated AERONET observations to within +0.005/-0.025. Thus, we note an overall low bias of 0.011 to 0.017, depending on wavelength. Traditionally, low AOD conditions over land were some of the most difficult situations for standard operational aerosol retrieval algorithms applied to orbiting radiometers. For example, the MODIS Dark Target algorithm reports an

530   accuracy at a low loading of ±0.05 (Levy et al., 2013), MODIS Deep Blue ±0.03 (Sayer et al., 2013), MISR ±0.03 to ±0.05 (Kahn et al., 2010). The radiometer products all expect twice the uncertainty at the low loading end than what was obtained from AirHARP/GRASP in these circumstances. Granted that these results were achieved for only seven AirHARP overpasses of AERONET sites and will need to be reproduced in a variety of settings and situations, but for now, the match-ups with AERONET are very promising for AOD retrievals over complex land surfaces.

535

GRASP was applied to AirHARP observations of two heavy aerosol loading situations, both of smoke plumes near fire sources. It is in these situations that GRASP was able to retrieve optical and microphysical characteristics of the smoke, in addition to AOD. Retrievals of smoke properties on the 27th October 2017 T18:16 UTC show that particles are fine with the real and imaginary refractive index of 1.55 and 0.024 respectively. Single scattering albedo of 0.87, 0.86, 0.84, and 0.81 are retrieved

540   for the smoke at 440 nm, 550 nm, 670 nm, and 870 nm respectively with volume median radius of 0.157 μm and standard deviation of 0.55 μm with a mixture of spherical and non-spherical particles. The isolated location of these local smoke plumes prevents any validation with AERONET observations. However, the retrieved optical and microphysical properties fall within expectations of fire smoke from previous publications, including a report from another ACEPOL polarimeter flying on the same aircraft as AirHARP. See the discussion in Section 5. Furthermore, the AirHARP/GRASP retrieved AOD agrees well

545   with collocated HSRL2 observations of the smoke plume to the degree to which the two sensors with very different observation geometries and cross-track pixel sizes can be matched. Note that when the plume is highly heterogeneous, the 3D structure of the plume must be accounted for in the polarimeter multi-angle vs. lidar nadir observations. This violates the plane-parallel aerosol layer assumption and will result in an AOD bias depending on the location of the measurement in the plume. Also, the smaller cross-track footprint of HSRL2 measurements, relative to AirHARP, adds complexity in the intercomparison.

550

AirHARP is the first manifestation of the HARP concept that makes multi-wavelength, hyper-angle, polarization measurements across a wide swath. Thus, the encouraging results demonstrated here show that when combined with GRASP inversion methods, HARP measurements can be used to retrieve highly accurate measures of AOD and aerosol optical/microphysical characteristics over a broad area. HARP Cubesat that will fly at the International Space Station orbit of

555   ~410 km in 2020 will cover ~1348 km in its across-track image, while HARP2 that will part of the Plankton, Aerosol, Clouds, ocean Ecosystem (PACE) mission at ~676 km orbit will image ~1550 km across its swath. This AirHARP/GRASP demonstration reinforces high expectations for these future HARP space missions. Furthermore, HARP has the potential to provide new characterization for clouds (Mcbride et al., 2020) and surface properties over various surface types, land and ocean. These new capabilities for aerosol, cloud and surface characterization will offer the community new insight into

560   important climate processes, public health issues and other societal concerns.

Appendix A

A.1 Land surface models

GRASP includes multiple land and ocean surface reflectance models. Here we will be discussing only the one we have used

565 for the retrievals in this paper. Land reflectance BRDF and BPDF models are derived using analytical (Cook et al., 2004; Rahman et al., 1993; Roujean et al., 1992; Wanner et al., 1995) and semi-empirical concept (Breon and Maignan, 2017), which used the heritage data from MODIS, POLDER to characterize the BRDF and BPDF models with higher accuracy. Currently, we use three land models for the retrievals.

A.1.1. Rahman-Pinty-Verstraete (RPV) BRDF model

570

This model uses only three parameters to express the directional reflectance from the surface which is illuminated from a direction (ϑ_1, ϕ_1) and observed from a direction (ϑ_2, ϕ_2) is given by,

$$\rho_{\text{RPV}}(\lambda, \vartheta_1, \phi_1, \vartheta_2, \phi_2) = \rho_0(\lambda) \frac{(\cos\vartheta_1 \cos\vartheta_2)^{k-1}}{(\cos\vartheta_1 + \cos\vartheta_2)^{1-k}} F(g) \left(1 + \frac{1 - \rho_0}{1 + G}\right) \qquad (A.1.1)$$

Where ρ_0 and k are two empirical surface parameters. $\left(1 + \frac{1-\rho_0}{1+G}\right)$ is an approximation of the hot spot effect.

$$F(g) = \frac{1 - \Theta^2}{[1 + \Theta^2 - 2\Theta \cos(\pi - g)]^{1.5}} \qquad (A.1.2)$$

F(g) is the Henyey-Greenstein phase function, where Θ, the function parameter which controls the relative amount of forward

575 and backward scattering. The phase angle g in Eq A.1.2 is given by

$$\cos(g) = \cos\vartheta_1 \cos\vartheta_2 + \sin\vartheta_1 \sin\vartheta_2 \cos(\phi_1 - \phi_2) \qquad (A.1.3)$$

When $\theta_1 = \theta_2$ and $\phi_1 = \phi_2$, i.e., in the hot spot, G = 0 and $\frac{1-\rho_0}{1+G}$ becomes maximum and total reflectance is increased. The equations Eq A.1.1 to Eq A.1.3 describe the anisotropy of the reflectance surface and can be represented by using three parameters ρ_0, k and Θ

A.1.2. Ross-Li BRDF model

580 This model characterizes the directional surface reflectance by the linear combination of three types of scattering kernels and is given by,

$$\rho_{Ross-Li}(\vartheta_1, \phi_1, \vartheta_2, \phi_2) = f_{iso}(\lambda) + K_{vol}(\lambda) f_{vol}(\vartheta_1, \phi_1, \vartheta_2, \phi_2) + K_{geo}(\lambda) f_{geo}(\vartheta_1, \phi_1, \vartheta_2, \phi_2) \qquad (A.1.4)$$

f_{iso}, f_{vol} and f_{geo} are the three kernels which represent isotropic, volumetric and geometric-optical surface scattering respectively. Litvinov et al., 2011 show that the surface reflectance can be represented as a product of geometrical and wavelength-dependent terms.

$$R_I(\vartheta_1, \phi_1, \vartheta_2, \phi_2, \lambda) \approx k(\lambda) f_i(\vartheta_1, \phi_1, \vartheta_2, \phi_2) \qquad (A.1.5)$$

585   From Eq A.1.4, Eq A.1.5 we can derive R as,

$$R_I(\vartheta_1, \phi_1, \vartheta_2, \phi_2, \lambda) = k(\lambda)\left[1 + k_1 f_{geo}(\vartheta_1, \phi_1, \vartheta_2, \phi_2) + k_2 f_{vol}(\vartheta_1, \phi_1, \vartheta_2, \phi_2)\right] \quad \text{(A.1.6)}$$

Where k_1 and k_2 are wavelength-independent linear model parameters for geometrical-optical and volumetric surface scattering kernels respectively. The $k(\lambda)$ is a wavelength-dependent model parameter.

A.1.3. Maignan-Breon BPDF model

Most of the theoretical models developed for the BPDF are based on the Fresnel equation of light reflection from a surface.

590   Nadal-Breon model uses two parameters non-linear Fresnel function to characterize the aerosol over land polarized reflectance. The polarized reflectance can be given by,

$$R_P(\vartheta_1, \phi_1, \vartheta_2, \phi_2) = \alpha\left(1 - exp\left(-\beta\frac{F_p(m, \gamma)}{cos\vartheta_1 + cos\vartheta_2}\right)\right) \quad \text{(A.1.7)}$$

where F_p is the polarized Fresnel reflection coefficient and is given by,

$$F_p = \frac{1}{2}(r^2_\perp + r^2_\parallel) \quad \text{(A.1.8)}$$

where $r_\perp$ and $r_\parallel$ are perpendicular and parallel components of Fresnel reflection coefficients respectively. Maignan et al., 2009 implemented a simple one-parameter model compared to the complicated two-parameter Nadal-Breon model to represent the

595   polarized reflectance from aerosol over the land surface. It has been used in the POLDER/PARASOL retrieval algorithm as a primary model for the BPDF over land. The one parameter BPDF model is given by,

$$R_P(\vartheta_1, \phi_1, \vartheta_2, \phi_2) = \frac{\alpha exp(-\tan\theta_r)F_p(m, \gamma)}{4(cos\vartheta_1 + cos\vartheta_2)} \quad \text{(A.1.9)}$$

Here α is the only free linear parameter. Θ_r is the angle of specular reflection.

A.2 Ocean surface models

For the surface model in the RT calculation, we used a modified cox-Munk isotropic model. A detailed description of this can

600   be found in references (Kawata et al., 1995; Mishchenko and Travis, 1997; Sun and Lukashin, 2013). The modified Cox-Munk model calculates the BRDF and BPDF based on three parameters, a_0 is the albedo of the ocean surface, which is spectrally dependent and smooth. a_1 is the fraction of Fresnel's reflection surface and a_2 is the variance of wind speed distribution. Wind speed distribution is given by the equation,

$$p(Z_x, Z_y) = \frac{1}{\pi a_2} exp\left(-\frac{Z_x^2 + Z_y^2}{a_2^2}\right) \quad \text{(A.2.1)}$$

Where,

$$a_2^2 = 0.003 + 0.00512V \quad \text{(A.2.2)}$$

605   Z_x, Z_y are X and Y slope components. V is the surface wind speed in m/s.

Appendix B

B.1 Aerosol Optical Depth calculation

In GRASP, atmospheric aerosol particles are considered as a mixture of spherical and randomly oriented spheroid particles and the aerosol optical depth is modeled as follows:

$$\tau_{aero}(\lambda) = \tau_{spherical}(\lambda) + \tau_{spheroid}(\lambda) \tag{B.1.1}$$

$$\tau_{spherical}(\lambda) = \int_{lnr_{min}}^{lnr_{max}} \frac{C_{ext}^{sphere}(\lambda, n, k, r)}{v(r)} \frac{dV(r)}{dln(r)} d(ln(r)) \tag{B.1.2}$$

610 And,

$$\tau_{spheroid}(\lambda) = \int_{ln\varepsilon_{min}}^{ln\varepsilon_{max}} \int_{lnr_{min}}^{lnr_{max}} \frac{C_{ext}^{\varepsilon}(\lambda, n, k, r)}{v(r)} \frac{dn(\varepsilon)}{dln(\varepsilon)} \frac{dV(r)}{dln(r)} d(ln(r)) d(ln(\varepsilon)) \tag{B.1.3}$$

where λ is the wavelength, n is the real part of the refractive index, k is the imaginary part of refractive index, $v(r)$ is the volume of particle, C_{ext}^{sphere} and $C_{ext}^{spheroid}$ are extinction cross-section of spherical and spheroid particles with aspect ratio ε($\varepsilon = \frac{a}{b}$, a is the axis of spheroid rotational symmetry, b is the axis perpendicular to the axis of spheroid rotational symmetry) respectively. $\frac{dn(\varepsilon)}{dln(\varepsilon)}$ used in GRASP is a fixed shape distribution as mentioned in Dubovik et al., 2006. Integrals in the Equation

615 B.1.2, Equation B.1.3 are changed to sum in order to do the computation fast and accurate and thus it becomes,

$$\tau_{spherical}(\lambda) = \sum_{i=1}^{N_r} \left(SF \times K_\tau^{spherical}(\lambda, n, k, r) \right) \frac{dV(r_i)}{dln(r)} \tag{B.1.4}$$

Where SF is the spherical fraction, K is the quadrature coefficient of extinction and is pre-computed kernels. Precomputed K has been calculated for a wide range of n ($1.33 \leq n \leq 1.7$) and k ($0.0001 \leq k \leq 0.5$). The calculations were done for a fixed aspect ratio from 0.3 to 3.0 and narrow size bins cover the size parameter range from ~0.0012 to ~625.

$$T_{spheroid}(\lambda) = \sum_{i=1}^{N_r} (1 - SF) K_\tau^{spheroid} \frac{dV(r_i)}{dln(r)} \tag{B.1.5}$$

Also,

$$\frac{dV_i(r)}{dln(r)} = \sum_{i=1,..,N} \frac{C_{v,i}}{\sqrt{2\pi}\sigma_i} exp\left(\frac{-(lnr - lnr_{v,i})^2}{2\sigma_i^2} \right) \tag{B.1.6}$$

620 $C_{v,i}$ is the concentration of different modes, $r_{v,i}$ is the volume median radius of each modes, and σ_i is the standard deviation.

Data availability

The AirHARP L1B and HSRL2 data for the ACEPOL campaign can be accessed from the website https://www-air.larc.nasa.gov/cgi-bin/ArcView/acepol. Quick look images for each of the AirHARP flights legs can be accessed through

625 the website https://sites.google.com/view/airharp-acepol/home. AERONET data used for this study can be download from https://aeronet.gsfc.nasa.gov/.

Author contribution

AP designed and implemented the study and analysis. AP wrote the manuscript with significant contributions from LR. BM, HM, and VM managed the operation of AirHARP instrument during the ACEPOL campaign. VM, BM, XX, and HB calibrated

630 and developed a scheme to generate the L1B data, which is the input for this data analysis. OD and PL helped with the retrievals by providing the GRASP software and support. SB has provided input for the HSRL2 – AirHARP AOD comparison. All the authors contributed towards the improvement of manuscript with valuable comments and suggestions.

Competing interests

The authors declare that they have no conflict of interest.

635 **Acknowledgement**

We thank the ACEPOL organizing team for supporting the involvement of AirHARP instrument in the project. We thank the PIs of the AERONET stations used in this study for maintaining and providing the easy access of data. We also acknowledge the engineering contributions from Dr. Fernadez-Borda (ESI, UMBC), and Mr. D. Cieslak (ESI, UMBC) in designing and manufacturing of AirHARP instrument. The authors acknowledge the support Dr. Lopatin (GRASP -SAS) and Dr. Lapionak

640 (LOA Université Lille) in providing the GRASP kernels for this study. The authors acknowledge the work by Python Software Foundation (http://www.python.org) and Anaconda Inc. (https://www.anaconda.com/) for developing and maintaining the python programming language and packages used for analysing and visualizing the data used in this study.

Financial support

This research is primarily supported through the NASA projects: HARP Cubesat (NNX13AN11G), AirHARP

645 (NNX16AK36G), and JCET cooperative agreement (NNX15AT34A). This research is also supported by the National Key R&D Program of China (Grant 2016YFE0201400). O. Dubovik appreciates support from the Chemical and Physical Properties of the Atmosphere Project funded by the French National Research Agency through the Programme d'Investissement d'Avenir

under contract ANR-11-LABX-0 0 05-01, the Regional Council "Hauts-de-France", and the "European Funds for Regional Economic Development". Barbosa acknowledges the support of processo nº 2016/18866-2, Fundação de Amparo à Pesquisa do Estado de São Paulo (FAPESP); and of project 308682/2017-3, Conselho Nacional de Desenvolvimento Científico e Tecnológico (CNPq).

650

Figures

(a)

26.55cm

42.67cm

(b)
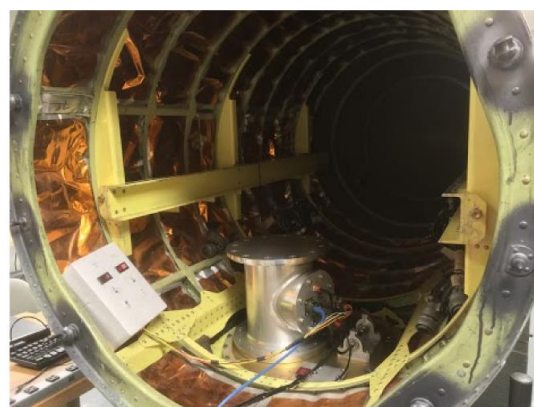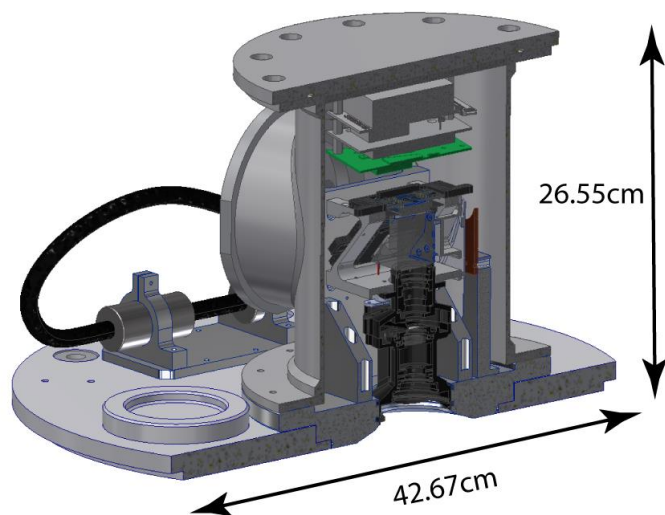
AirHARP instrument mounted on the
front pod of the ER-2 aircraft's left-wing

(c)

Figure 1. (a) Cross-section image of AirHARP instrument rendered using CAD software; (b) AirHARP instrument mounted on ER-2 aircraft left-wing front pod (Image courtesy: Brent McBride); (c) Image captured by NASA Science Pilot D. Stuart Broce, during the ACEPOL flight on Oct-26 2017. The red arrow in the figure points to the AirHARP's exposed part when mounted on the wing pod.
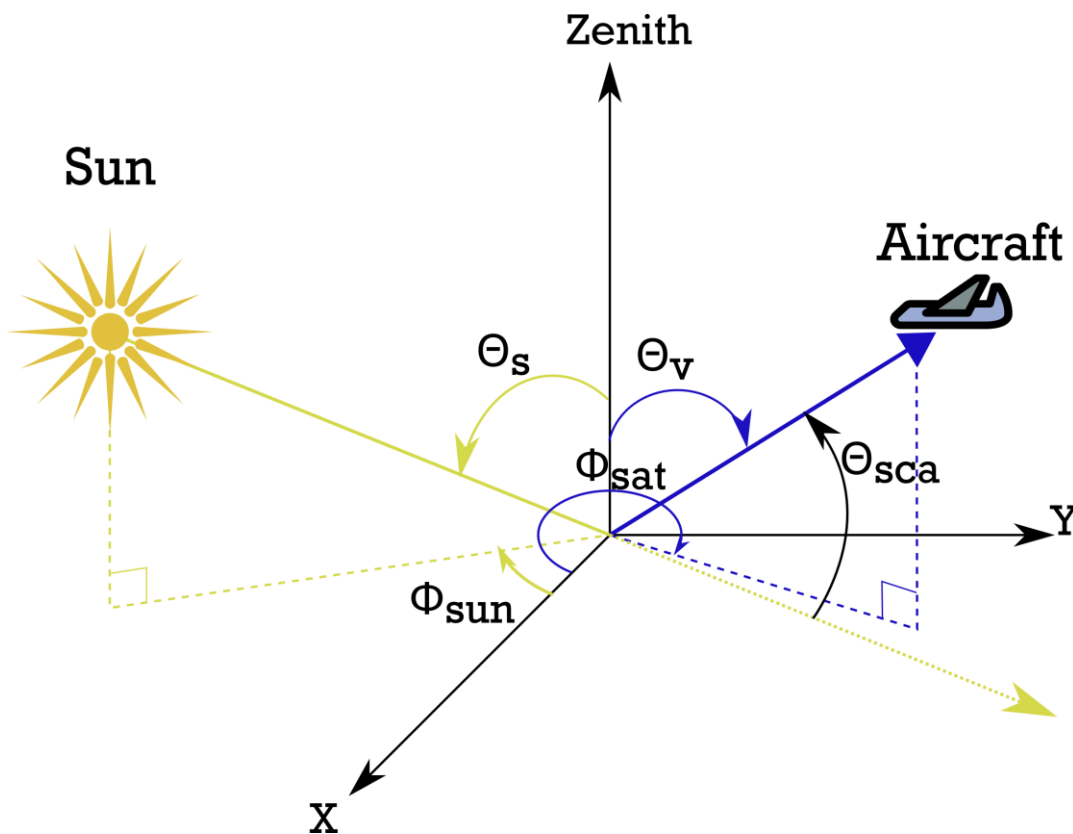
Figure 2. AirHARP viewing geometry and definition of angles. Θ_s **is the solar zenith angle,** Θ_v **is the viewing zenith angle,** Φ_{sun} **is** the solar azimuthal angle, Φ_{sat} **is the viewing azimuthal angle, and** Θ_{sca} **is the scattering angle. The point where X and Y coordinates meet is the local ground point.**

660
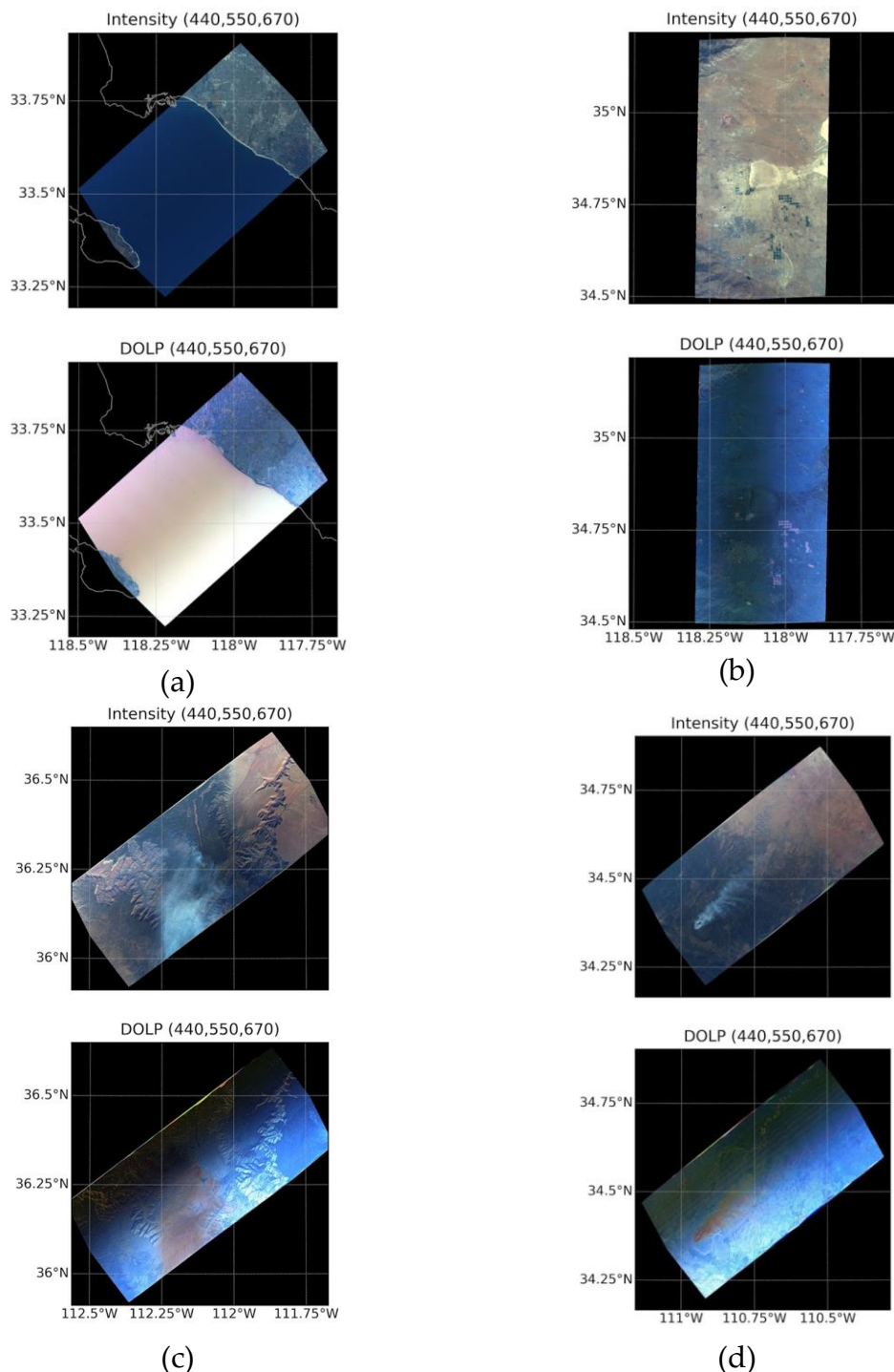
Figure 3. Nadir RGB (670 nm, 550 nm, and 440 nm) images of radiance and DoLP for the selected cases from AirHARP flight legs listed in Table 2. The X-axis is the longitude and the Y-axis the latitude. The scenes include (a) sun glint scene over the Pacific Ocean near Los Angeles, California, USA (23rd October 2017 T21:30 UTC); (b) Rosamond dry lake in California, USA, (25th October 2017

T18:26 UTC); (c) biomass burning scene near the Kaibab national forest and Grand Canyon national park, (27th October 2017 T18:16 UTC); (d) biomass burning scene near the Kaibab national forest(9th November 2017 T19:30 UTC).
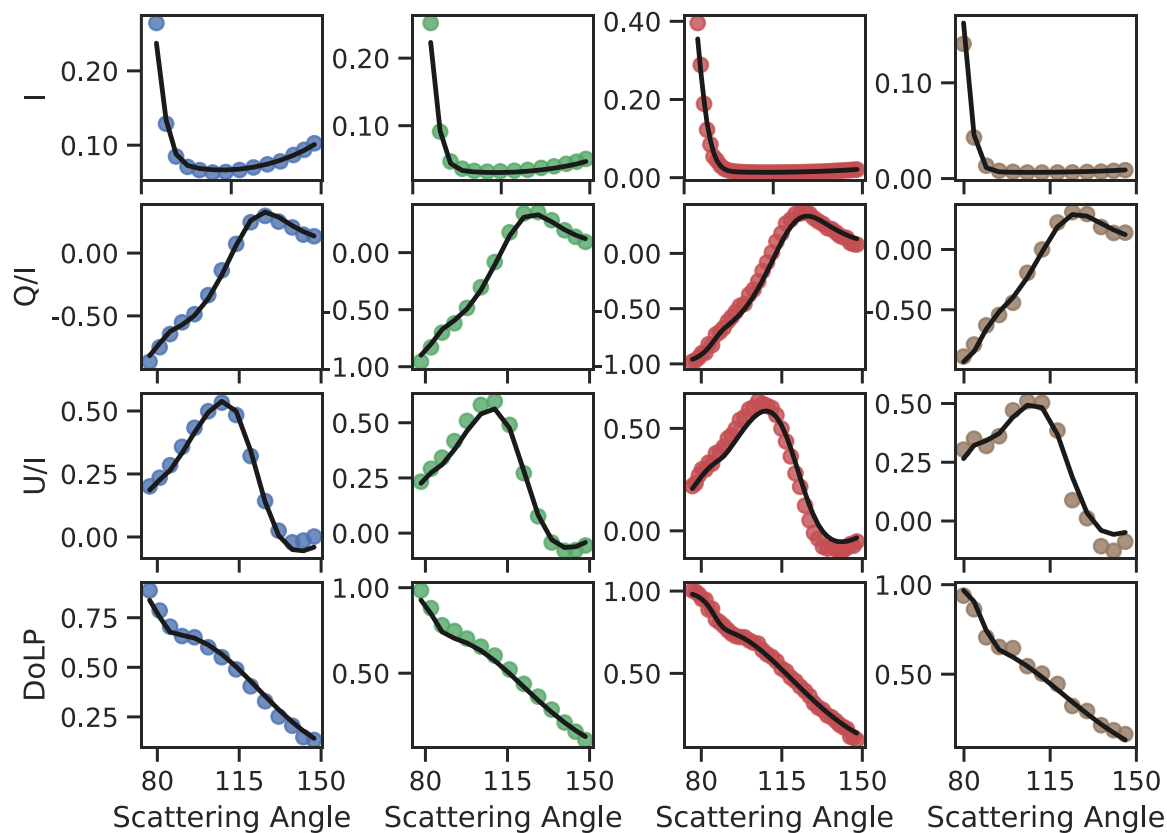
670   **Figure 4. AirHARP measured I, Q/I, U/I and DoLP (solid colored circles) for a single sun glint pixel from the scene in Fig. 3(a) and the GRASP fit to the measurements (black solid line) for all bands (Blue – 440 nm, Green -550 nm, Red – 670 nm and Brown- 870 nm)**

675

(j) (k) (l)
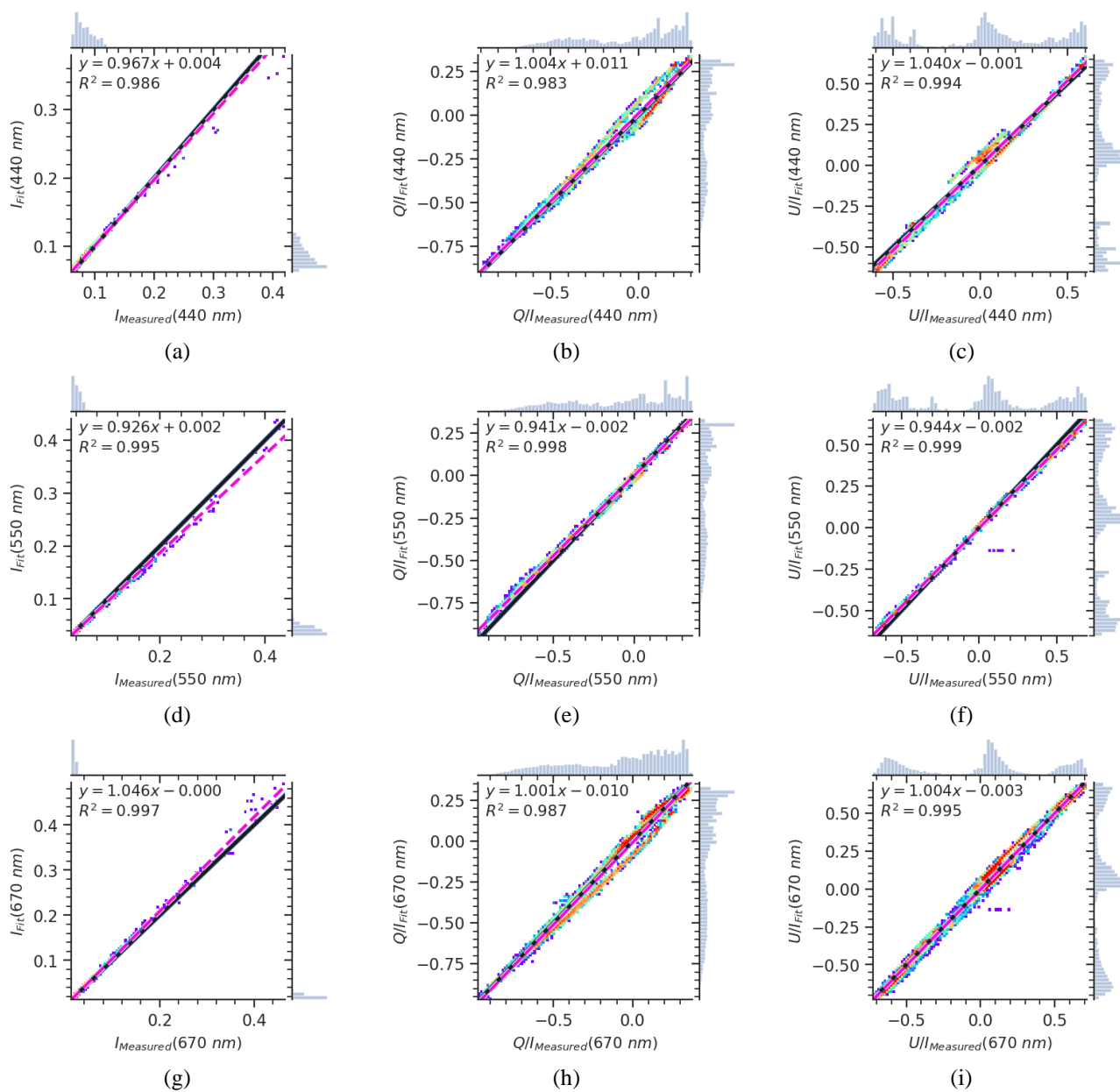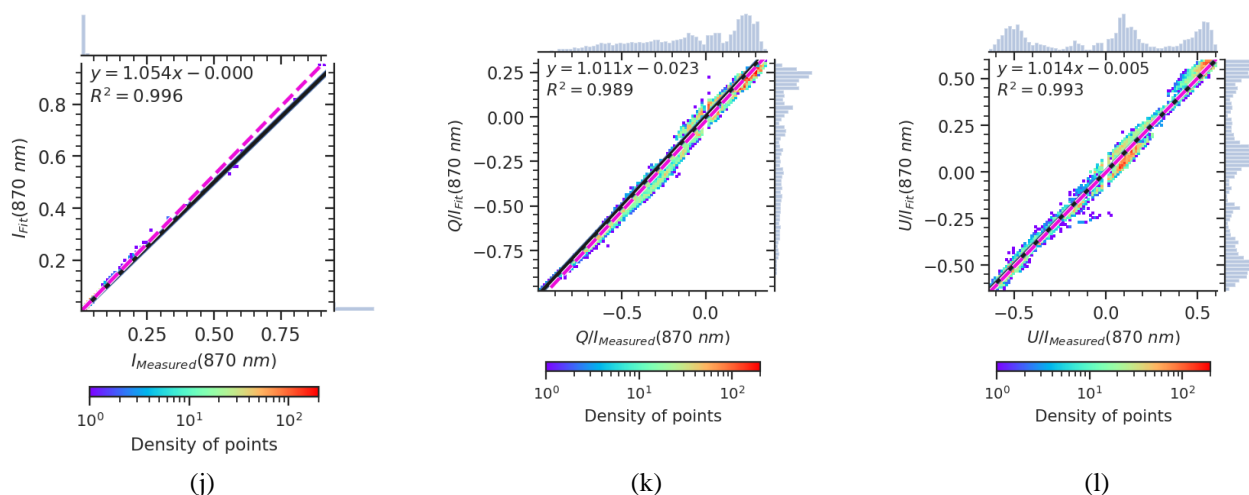
Figure 5. Scatter density plots for AirHARP measurement variables and GRASP fit for the ocean scene in Fig. 3(a). The subplots (a), (d), (g) and (j) are the 2D density plots for variable I at different spectral bands blue, green, red and NIR, respectively; (b), (e), (h) and (k) are for the variable Q/I; (c), (f), (i) and (l) are for the variable U/I. The dashed magenta line is the Ordinary Least Square (OLS) Fit for the measured and GRASP fitted variable. The solid black line is the 1:1 line for the measured and fitted variable. 680 **There are 72,000 data points for 440, 550, and 870 nm bands and 216,000 data points for the 670 nm band. For each plot, the histogram of measurement and GRASP fit for each variable are plotted on the top and right axis respectively.**
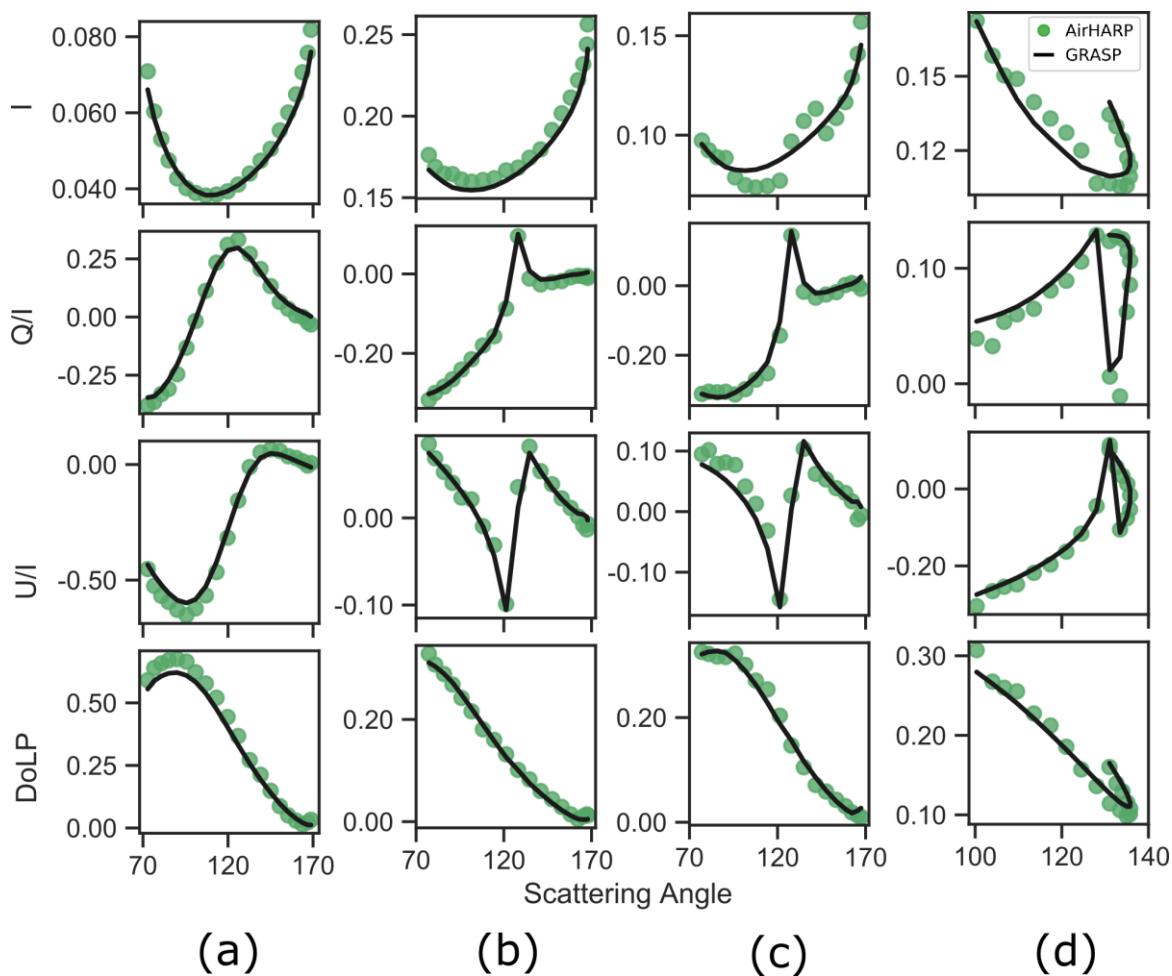
685 **Figure 6.** AirHARP measured I, Q/I, U/I and DoLP (solid colored circles) and the GRASP fit (black solid lines) for selected pixels from the scene in Fig. 3(a,b,c) are plotted for the 550 nm band. Column (a) an offglint pixel from the scene on 23 October 2017 T21:30 UTC; (b) for a dry lake pixel from the flight leg on 25 October 2017 T18:26 UTC; (c) for a vegetation surface also from flight leg on 25 October 2017 T18:26 UTC; (d) for a smoke pixel from flight leg on 27th October 2017 T18:16 UTC.
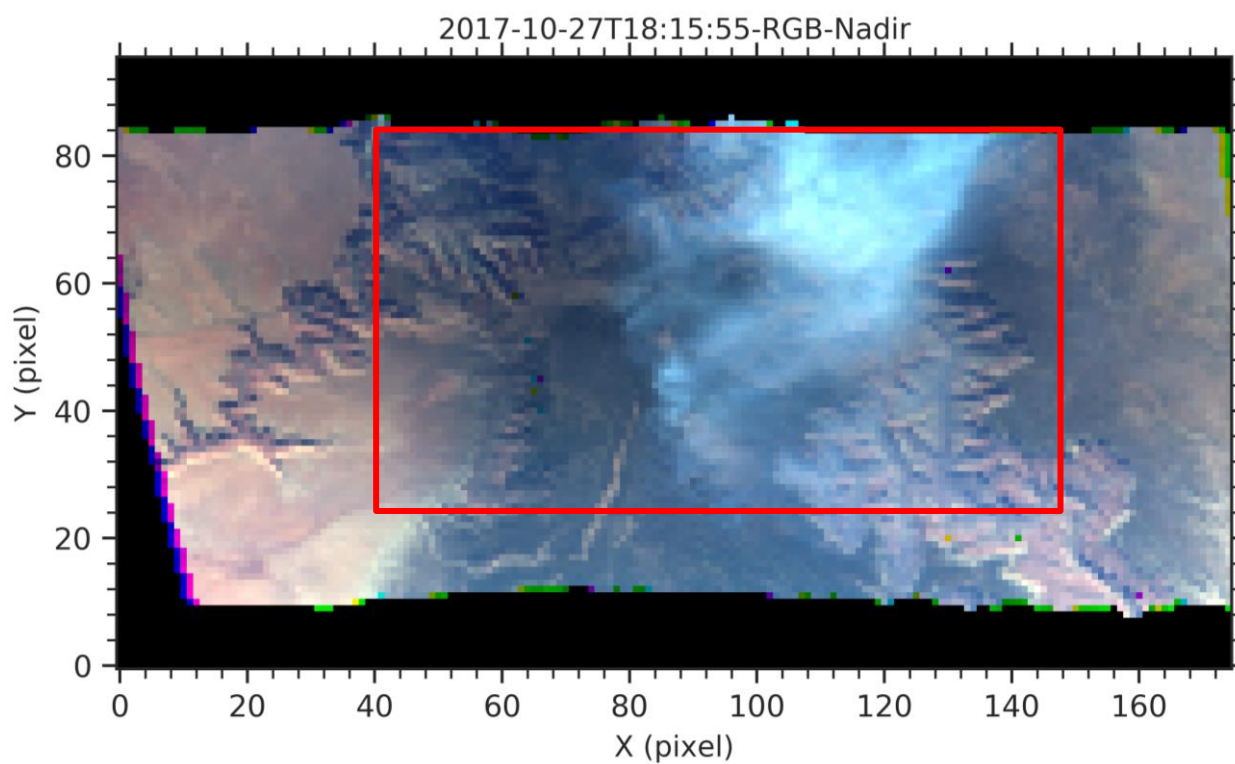
690 **Figure 7. RGB composite image of the 27th October 2017 T18:16 UTC smoke scene, X and Y axes are the number of pixels (550m x 550m) along the respective axes. Pixels inside the red rectangular box are used for the aerosol retrievals of AOD, SSA, RRI, IRI. These are plotted in Fig. 8.**
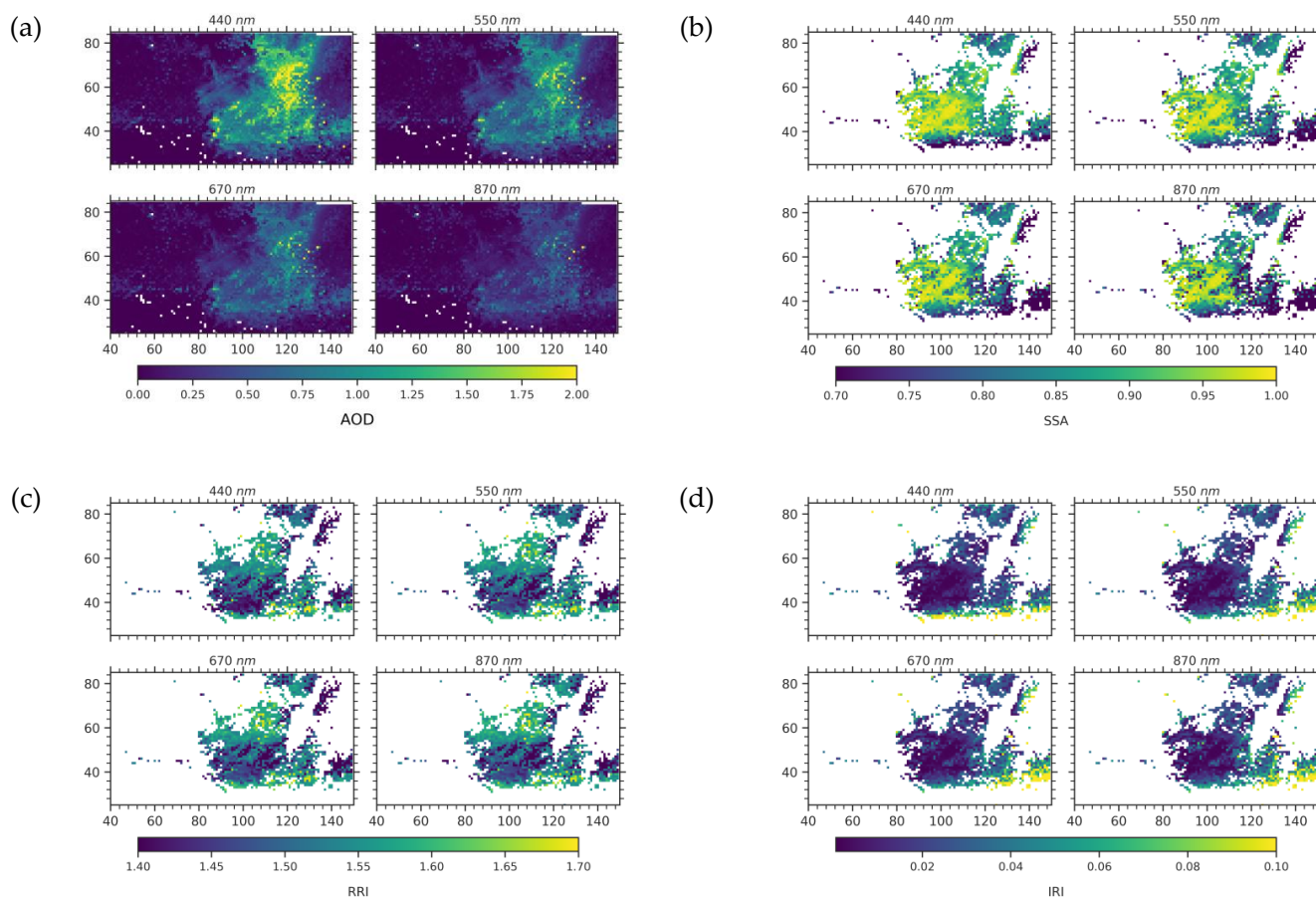
Figure 8. (a) AOD map of a subsetted portion of the 27th October 2017 T18:16 UTC smoke scene that was marked by a red rectangular box in Fig. 7; (b)
695 **Single Scatteing Albedo (SSA) for the same subsetted portion in (a) but the pixels with the goodness of fit, $\chi^2_{norm} > 5$ and $AOD_{440\,nm} < 0.4$ are masked.**
(c) same as (b) except the real part of the refractive index (RRI) is plotted. (d) same as (b) except the imaginary part of the refractive index (IRI) is plotted.
X and Y axes are the pixel coordinates
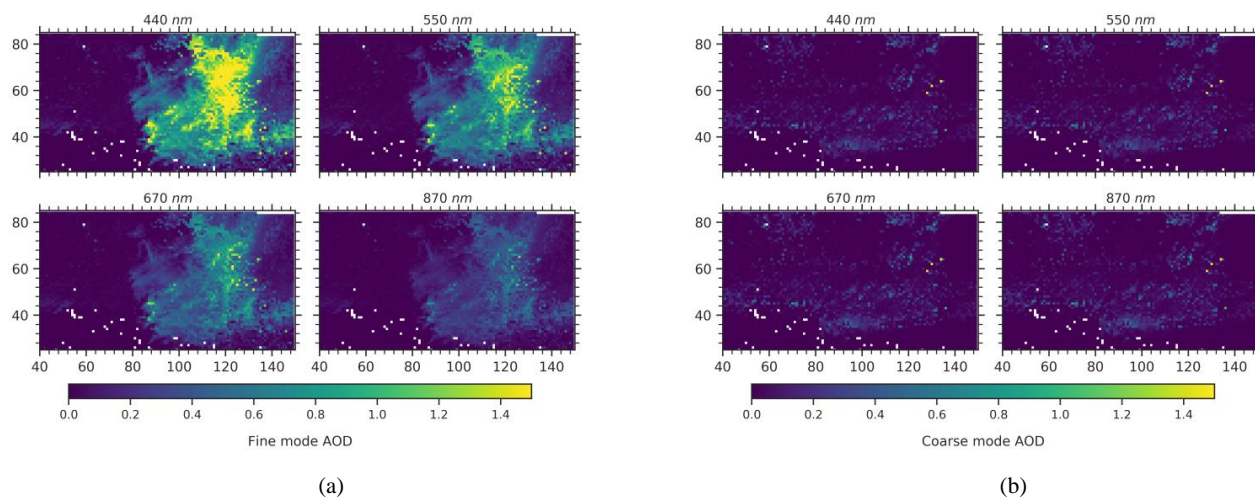
Figure 9. (a) Fine mode AOD map of a subsetted portion of the 27th October 2017 T18:16 UTC smoke scene that was marked by a red rectangular box in Fig. 7 for all AirHARP spectral bands; (b) same as (a) but for coarse mode AOD. X and Y axes are the pixel coordinates.
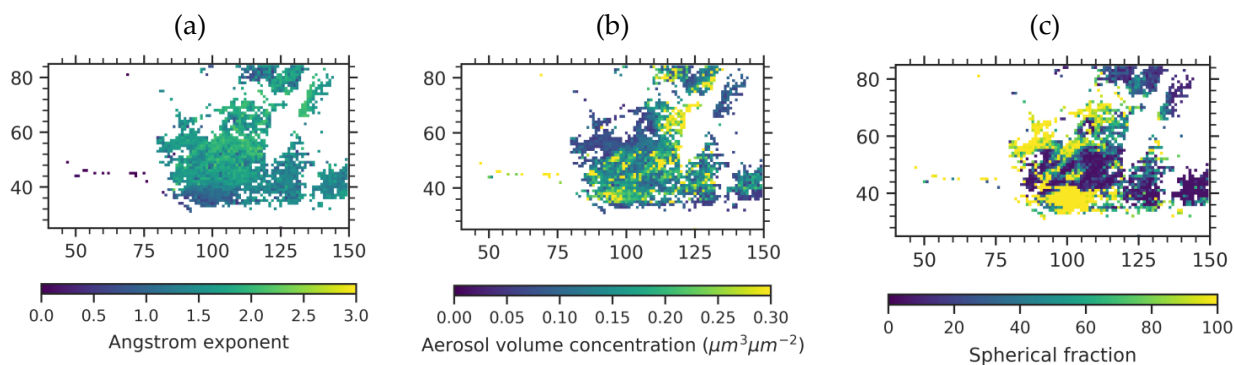
Figure 10. Map of (a) angstrom exponent (AE), (b) aerosol volume concentration, and (c) spherical fraction (SF) of the scene shown in Fig. 8. Pixel filtering similar to the one applied for SSA, RRI, and IRI in Fig. 8 is applied to filter out bad pixels from AE, aerosol volume concentration, and SF map. X and Y axes are the pixel coordinates.
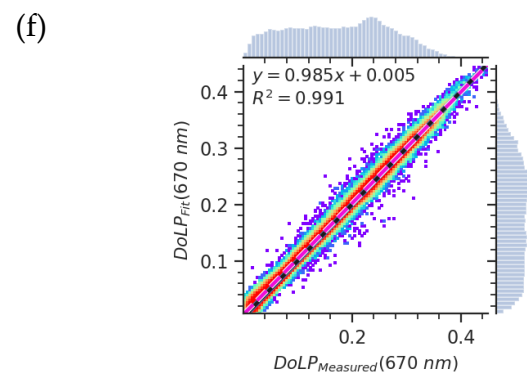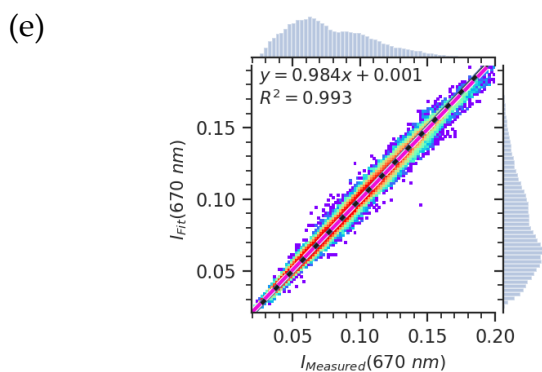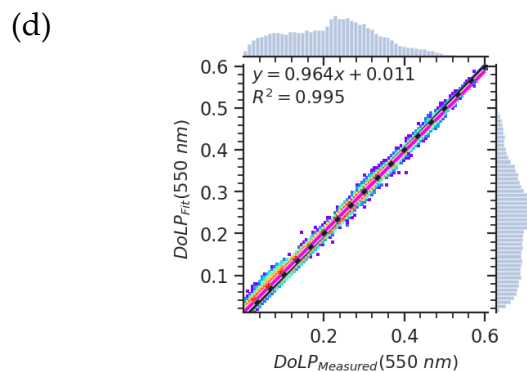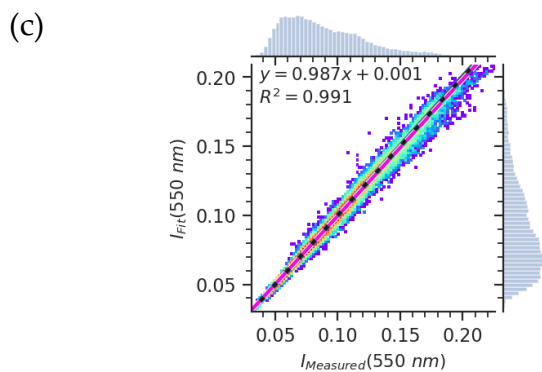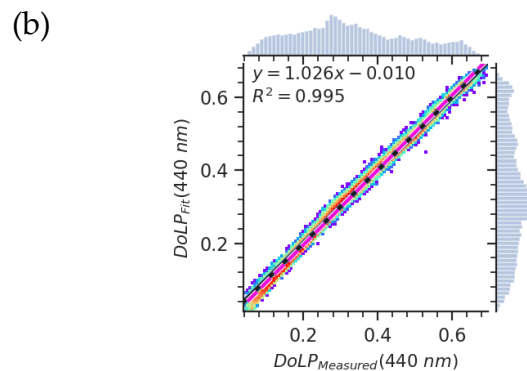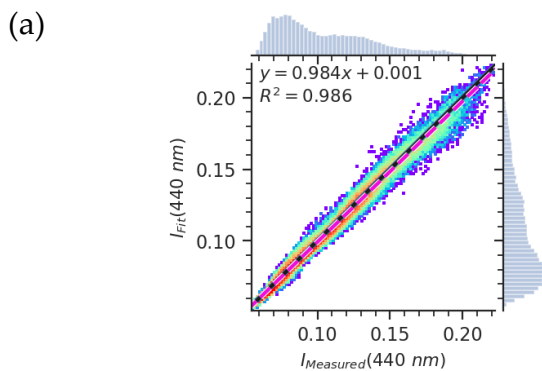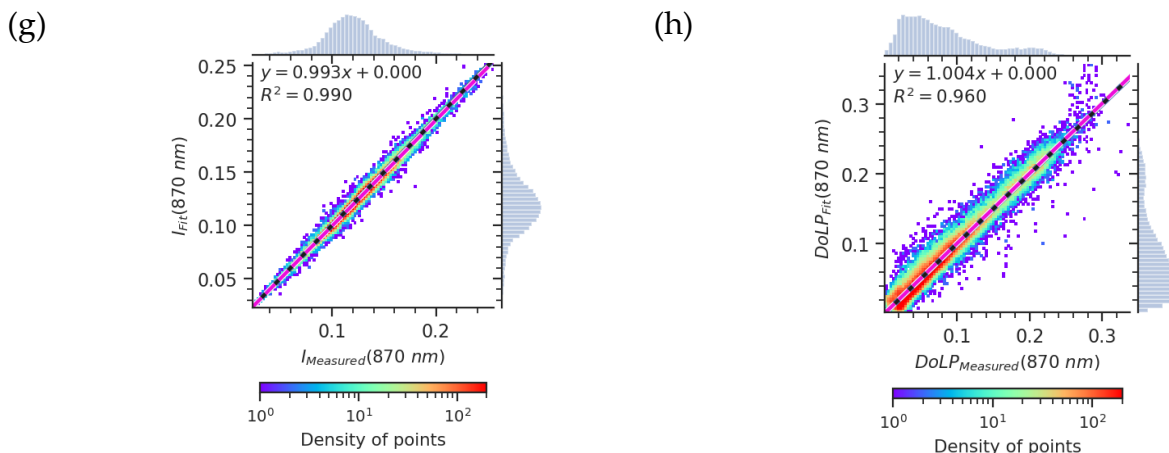
Figure 11. Scatter density plot for AirHARP measurement variables and GRASP fit for the scene in Fig. 8. 1:1 line (black solid line), Ordinary Least Square (OLS) regression line (magenta dashed line), the OLS fit parameters and correlation (R^2) are also reported in the same graph. For each plot, the histogram of measurement and GRASP fit for I and DoLP are plotted on the top and right axis respectively.
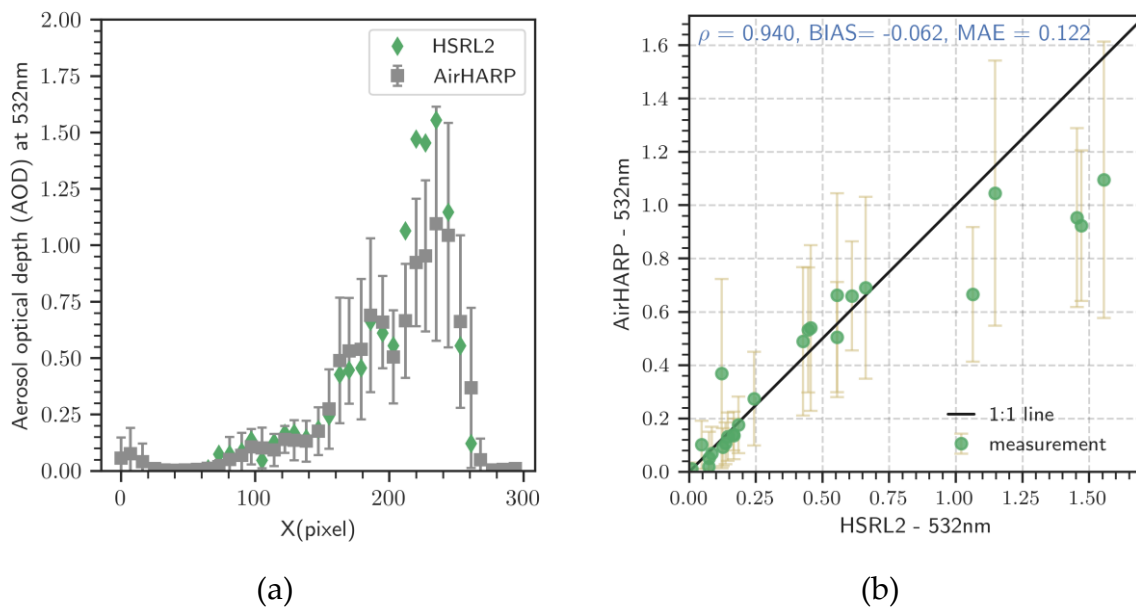
Figure 12. (a) AOD at 532 nm from AirHARP versus HSRL2 AOD at 532 nm along the flight track for the forest fire scene on 9th November 2017 T19:30 UTC; (b) Correlation plot for the HSRL2 AOD at 532 nm vs AirHARP AOD at 532 nm for the same flight.
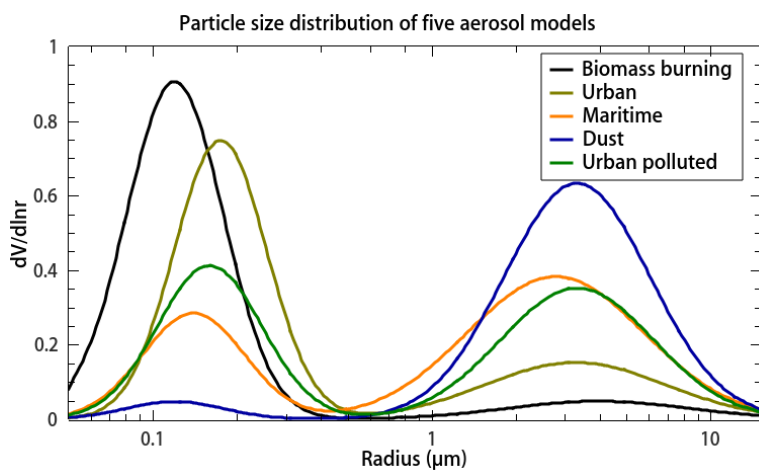
Figure 13. Particle size distribution of five aerosol types listed in the Table 6. This simplified aerosol component-based kernels are used for the AirHARP AOD inversion over the collocated AERONET pixels during ACEPOL 2017 campaign.

715
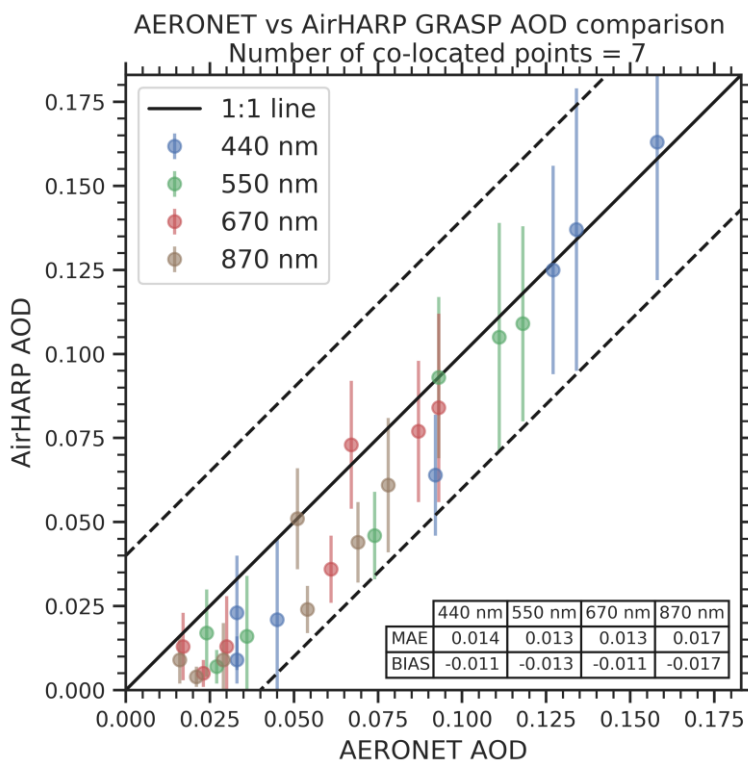
Figure 14. Scattergram of aerosol optical depth (AOD) retrieved using AirHARP observations over collocated AERONET pixels vs AERONET measured AOD interpolated at AirHARP spectral bands. A box of 5.5km x 5.5km around the collocated AERONET pixel is used to calculate the spatial mean AOD (solid colored circles) over AERONET station using the AirHARP AOD retrievals. Each colored error bars indicate the standard deviation of AOD within the matching box. Mean Absolute Error (MAE) and BIAS for each spectral band are provided in the table inside the scattergram. Black dashed lines in the plot are 1:1 line $\pm$ 0.04.

720

Tables

725 **Table 1: Information on AirHARP spectral bands, viewing angles, and measured parameters**

Band nominal wavelength	No. of viewing angles	Measured Variables
440 nm	20	I, Q, U
550 nm	20	I, Q, U
670 nm	60	I, Q, U
870 nm	20	I, Q, U

Table 2: Table of flights analyzed from the ACEPOL campaign which flew over the ocean, land, forest fire smoke, and AERONET sites.

Date of flight	Time of flights (UTC)	Target Type
23-October-2017	21:30-21:36	Ocean
23-October-2017	21:53-21:59	Aeronet Station (CalTech)
25-October-2017	18:26-18:32	Dry lake
25-October-2017	19:55-20:01	Aeronet Station (Bakersfield)
25-October-2017	20:21-20:27	Aeronet Station (Fresno_2)
26-October-2017	19:15-19:21	Aeronet Station (Bakersfield)
26-October-2017	21:24-21:32	Aeronet Station (Railroad Valley)
27-October-2017	18:16-18:22	Smoke over land
07-November-2017	19:36-19:42	Aeronet Station (Fresno_2)
09-November-2017	18:31-18:37	Aeronet Station (USGS_Flagstaff)
09-November-2017	19:31-19:37	Smoke over land

Table 3: Five log-normal modes used for particle size distribution in GRASP retrieval for AirHARP, r_v is the volume median radius, and σ_v, geometric standard deviation

$r_v(\mu m)$	$\log(\sigma_v)$
0.1	0.35
0.1732	0.35
0.3	0.35
1.0	0.5
2.9	0.5

Table 4: Definition of statistical parameters used in this study to find the correlation between measurement and models

Statistical Parameter	Mathematical Formulae
The goodness of fit (χ^2_{norm})	$\chi^2_{norm} = \dfrac{1}{N} \sum_{i=1}^{N} \dfrac{(y_i - x_i)^2}{S_y}$
Pearson Coefficient (ρ)	$\rho = \dfrac{\sum_{i=1}^{n}(x_i - \overline{x})(y_i - \overline{y})}{\sqrt{\sum_{i=1}^{n}(x_i - \overline{x})^2 \sum_{i=1}^{n}(y_i - \overline{y})^2}}$
Coefficient of Determination (R²)	$R^2 = \rho^2$
Mean Absolute Error (MAE)	$MAE = \dfrac{\sum_{i=1}^{N}(|y_i - x_i|)}{N}$
Bias	$BIAS = \overline{y} - \overline{x}$

Table 5: Mean aerosol optical and microphysical properties retrieved for the smoke scene in Fig. 8 (for pixels with AOD$_{440\ nm}$ > 0.4).

Spectral Band	Single Scattering Albedo	Spherical Fraction (%)	Angstrom Exponent[#]	Real Refractive Index (RRI)	Imaginary Refractive Index (RRI)
440 nm	0.870				
550 nm	0.855	49.9%[@]	1.53	1.55	0.024
670 nm	0.838				
870 nm	0.812				

[#]Angstrom Exponent calculated using the AOD at wavelength bands 440 nm and 870 nm of the AirHARP

[@]Retrieved spherical fraction includes significant number of pixels with SF ~ 99%

Table 6: Details on the complex refractive index, and particle size distribution parameters used for the aerosol models. C_v, is the concentration, $\ln(\sigma_v)$ is the standard deviation of the distribution, and r_v is the volume median radius. Fine and coarse mode
745 **parameters are indicated by *f* and *c* subscripts respectively.**

Aerosol models	Real part of the refractive index (RRI)	Imaginary part of the refractive index (IRI) (440 nm, 550 nm, 670 nm, 870 nm)				$C_{v,f}$	$\ln(\sigma_{v,f})$	$r_{v,f}$	$C_{v,c}$	$\ln(\sigma_{v,c})$	$r_{v,c}$
Biomass	1.510		0.050			0.91	0.40	0.120	0.09	0.75	3.95
Urban	1.395		0.003			0.75	0.38	0.018	0.30	0.75	3.27
Urban polluted	1.470		0.100			0.52	0.43	0.160	0.48	0.63	3.32
Maritime	1.370		0.0001			0.30	0.42	0.140	0.70	0.73	2.78
Dust	1.560	0.0029	0.0019	0.0013	0.0011	0.02	0.40	0.120	0.40	0.60	3.32

References

Benavent-Oltra, J. A., Román, R., Casquero-Vera, J. A., Pérez-Ramírez, D., Lyamani, H., Ortiz-Amezcua, P., Bedoya-Velásquez, A. E., de Arruda Moreira, G., Barreto, Á., Lopatin, A., Fuertes, D., Herrera, M., Torres, B., Dubovik, O., Guerrero-Rascado, J. L., Goloub, P., Olmo-Reyes, F. J. and Alados-Arboledas, L.: Different strategies to retrieve aerosol properties at night-time with the GRASP algorithm, Atmos. Chem. Phys., 19(22), 14149–14171, doi:10.5194/acp-19-14149-2019, 2019.

Bergstrom, R. W., Pilewskie, P., Russell, P. B., Redemann, J., Bond, T. C., Quinn, P. K. and Sierau, B.: Spectral absorption properties of atmospheric aerosols, Atmos. Chem. Phys., 7(23), 5937–5943, doi:10.5194/acp-7-5937-2007, 2007.

Bond, T. C., Anderson, T. L. and Campbell, D.: Calibration and Intercomparison of Filter-Based Measurements of Visible Light Absorption by Aerosols, Aerosol Sci. Technol., 30(6), 582–600, doi:10.1080/027868299304435, 1999.

Boucher, O., Granier, C., Hoose, C. and Uk, A. J.: Clouds and aerosols, in Climate Change 2013 the Physical Science Basis: Working Group I Contribution to the Fifth Assessment Report of the Intergovernmental Panel on Climate Change, vol. 9781107057, edited by Intergovernmental Panel on Climate Change, pp. 571–658, Cambridge University Press, Cambridge., 2013.

Breon, F. M. and Maignan, F.: A BRDF-BPDF database for the analysis of Earth target reflectances, Earth Syst. Sci. Data, 9(1), 31–45, doi:10.5194/essd-9-31-2017, 2017.

Burton, S. P., Ferrare, R. A., Hostetler, C. A., Hair, J. W., Rogers, R. R., Obland, M. D., Butler, C. F., Cook, A. L., Harper, D. B. and Froyd, K. D.: Aerosol classification using airborne High Spectral Resolution Lidar measurements – methodology and examples, Atmos. Meas. Tech., 5(1), 73–98, doi:10.5194/amt-5-73-2012, 2012.

Burton, S. P., Hostetler, C. A., Cook, A. L., Hair, J. W., Seaman, S. T., Scola, S., Harper, D. B., Smith, J. A., Fenn, M. A., Ferrare, R. A., Saide, P. E., Chemyakin, E. V. and Müller, D.: Calibration of a high spectral resolution lidar using a Michelson interferometer, with data examples from ORACLES, Appl. Opt., 57(21), 6061, doi:10.1364/AO.57.006061, 2018.

Cairns, B., Russell, E. E. and Travis, L. D.: Research Scanning Polarimeter: calibration and ground-based measurements, in Polarization: Measurement, Analysis, and Remote Sensing II, vol. 3754, edited by D. H. Goldstein and D. B. Chenault, pp. 186–196., 1999.

Cairns, B., Russell, E. E., LaVeigne, J. D. and Tennant, P. M. W.: Research scanning polarimeter and airborne usage for remote sensing of aerosols, in Polarization Science and Remote Sensing, vol. 5158, edited by J. A. Shaw and J. S. Tyo, p. 33., 2003.

Chakrabarty, R. K., Moosmüller, H., Garro, M. A., Arnott, W. P., Walker, J., Susott, R. A., Babbitt, R. E., Wold, C. E., Lincoln, E. N. and Hao, W. M.: Emissions from the laboratory combustion of widland fuels: Particle morphology and size, J. Geophys. Res. Atmos., 111(7), 1–16, doi:10.1029/2005JD006659, 2006.

Chen, C., Dubovik, O., Henze, D. K., Lapyonak, T., Chin, M., Ducos, F., Litvinov, P., Huang, X. and Li, L.: Retrieval of desert dust and carbonaceous aerosol emissions over Africa from POLDER/PARASOL products generated by the GRASP algorithm, Atmos. Chem. Phys., 18(16), 12551–12580, doi:10.5194/acp-18-12551-2018, 2018.

Chen, C., Dubovik, O., Henze, D. K., Chin, M., Lapyonok, T., Schuster, G. L., Ducos, F., Fuertes, D., Litvinov, P., Li, L.,

780 Lopatin, A., Hu, Q. and Torres, B.: Constraining global aerosol emissions using POLDER/PARASOL satellite remote sensing observations, Atmos. Chem. Phys. Discuss., 14585–14606, doi:10.5194/acp-2019-623, 2019.

Chen, Y. and Penner, J. E.: Uncertainty analysis for estimates of the first indirect aerosol effect, Atmos. Chem. Phys., 5(11), 2935–2948, doi:10.5194/acp-5-2935-2005, 2005.

Cook, E. R., Woodhouse, C., Eakin, C. M., Meko, D. M. and Stahle, D. W.: Long-term aridity changes in the western United
785 States., Science, 306(5698), 1015–8, doi:10.1126/science.1102586, 2004.

Cox, C. and Munk, W.: Measurement of the Roughness of the Sea Surface from Photographs of the Sun's Glitter, J. Opt. Soc. Am., 44(11), 838, doi:10.1364/JOSA.44.000838, 1954.

Deuzé, J. L., Herman, M., Goloub, P., Tanré, D. and Marchand, A.: Characterization of aerosols over ocean from POLDER/ADEOS-1, Geophys. Res. Lett., 26(10), 1421–1424, doi:10.1029/1999GL900168, 1999.

790 Deuzé, J. L., Bréon, F. M., Devaux, C., Goloub, P., Herman, M., Lafrance, B., Maignan, F., Marchand, A., Nadal, F., Perry, G. and Tanré, D.: Remote sensing of aerosols over land surfaces from POLDER-ADEOS-1 polarized measurements, J. Geophys. Res. Atmos., 106(D5), 4913–4926, doi:10.1029/2000JD900364, 2001.

Diner, D. J., Abdou, W. A., Ackerman, T. P., Crean, K., Gordon, H. R., Kahn, R. A., Martonchik, J. V, McMuldroch, S., Paradise, S. R., Pinty, B. and others: MISR level 2 aerosol retrieval algorithm theoretical basis, JPL D-11400, Rev, G, Jet
795 Propul. Lab., Calif. Inst. Technol., Pasadena, CA, USA, online available eospso. gsfc. nasa. gov/eos homepage/for Sci., 2008.

Diner, D. J., Xu, F., Garay, M. J., Martonchik, J. V., Rheingans, B. E., Geier, S., Davis, A., Hancock, B. R., Jovanovic, V. M., Bull, M. A., Capraro, K., Chipman, R. A. and McClain, S. C.: The Airborne Multiangle SpectroPolarimetric Imager (AirMSPI): a new tool for aerosol and cloud remote sensing, Atmos. Meas. Tech., 6(8), 2007–2025, doi:10.5194/amt-6-2007-2013, 2013.

800 Dubovik, O.: Optimization of Numerical Inversion in Photopolarimetric Remote Sensing, Photopolarimetry Remote Sens., 65–106, doi:10.1007/1-4020-2368-5_3, 2006.

Dubovik, O. and King, M. D.: A flexible inversion algorithm for retrieval of aerosol optical properties from Sun and sky radiance measurements, J. Geophys. Res. Atmos., 105(D16), 20673–20696, doi:10.1029/2000JD900282, 2000.

Dubovik, O., King, M. D. and others: A flexible inversion algorithm for retrieval of aerosol optical properties from Sun and
805 sky radiance measurements, J. Geophys. Res. Atmos., 105(D16), 20673–20696, doi:10.1029/2000JD900282, 2000.

Dubovik, O., Holben, B., Eck, T. F., Smirnov, A., Kaufman, Y. J., King, M. D., Tanré, D. and Slutsker, I.: Variability of Absorption and Optical Properties of Key Aerosol Types Observed in Worldwide Locations, J. Atmos. Sci., 59(3), 590–608, doi:10.1175/1520-0469(2002)059<0590:VOAAOP>2.0.CO;2, 2002.

Dubovik, O., Sinyuk, A., Lapyonok, T., Holben, B. N., Mishchenko, M., Yang, P., Eck, T. F., Volten, H., Muñoz, O.,
810 Veihelmann, B., van der Zande, W. J., Leon, J. F., Sorokin, M. and Slutsker, I.: Application of spheroid models to account for aerosol particle nonsphericity in remote sensing of desert dust, J. Geophys. Res. Atmos., 111(11), doi:10.1029/2005JD006619, 2006.

Dubovik, O., Herman, M., Holdak, A., Lapyonok, T., Tanré, D., Deuzé, J. L., Ducos, F., Sinyuk, A. and Lopatin, A.:

Statistically optimized inversion algorithm for enhanced retrieval of aerosol properties from spectral multi-angle polarimetric

815   satellite observations, 2011.

Dubovik, O., Lapyonok, T., Litvinov, P., Herman, M., Fuertes, D., Ducos, F., Lopatin, A., Chaikovsky, A., Torres, B.,
Derimian, Y. and others: GRASP: a versatile algorithm for characterizing the atmosphere, in Proc. SPIE., 2014.

Dubovik, O., Li, Z., Mishchenko, M. I., Tanré, D., Karol, Y., Bojkov, B., Cairns, B., Diner, D. J., Espinosa, W. R., Goloub,
P., Gu, X., Hasekamp, O., Hong, J., Hou, W., Knobelspiesse, K. D., Landgraf, J., Li, L., Litvinov, P., Liu, Y., Lopatin, A.,

820   Marbach, T., Maring, H., Martins, V., Meijer, Y., Milinevsky, G., Mukai, S., Parol, F., Qiao, Y., Remer, L., Rietjens, J., Sano,
I., Stammes, P., Stamnes, S., Sun, X., Tabary, P., Travis, L. D., Waquet, F., Xu, F., Yan, C. and Yin, D.: Polarimetric remote
sensing of atmospheric aerosols: Instruments, methodologies, results, and perspectives, J. Quant. Spectrosc. Radiat. Transf.,
224, 474–511, doi:10.1016/j.jqsrt.2018.11.024, 2019.

Emde, C., Barlakas, V., Cornet, C., Evans, F., Korkin, S., Ota, Y., Labonnote, L. C., Lyapustin, A., Macke, A., Mayer, B. and

825   Wendisch, M.: IPRT polarized radiative transfer model intercomparison project - Phase A, J. Quant. Spectrosc. Radiat. Transf.,
164, 8–36, doi:10.1016/j.jqsrt.2015.05.007, 2015.

Espinosa, W. R., Remer, L. A., Dubovik, O., Ziemba, L., Beyersdorf, A., Orozco, D., Schuster, G., Lapyonok, T., Fuertes, D.
and Martins, J. V.: Retrievals of aerosol optical and microphysical properties from Imaging Polar Nephelometer scattering
measurements, Atmos. Meas. Tech., 10(3), 811–824, doi:10.5194/amt-10-811-2017, 2017.

830   Espinosa, W. R., Martins, J. V., Remer, L. A., Puthukkudy, A., Orozco, D. and Dolgos, G.: In situ measurements of angular-
dependent light scattering by aerosols over the contiguous United States, Atmos. Chem. Phys., 18(5), 3737–3754,
doi:10.5194/acp-18-3737-2018, 2018.

Fernandez-Borda, R., Waluschka, E., Pellicori, S., Martins, J. V., Ramos-Izquierdo, L., Cieslak, J. D. and Thompson, P.:
Evaluation of the polarization properties of a Philips-type prism for the construction of imaging polarimeters, in Polarization

835   Science and Remote Sensing IV, vol. 7461, edited by J. A. Shaw and J. S. Tyo, p. 746113., 2009.

Fougnie, B., Marbach, T., Lacan, A., Lang, R., Schlüssel, P., Poli, G., Munro, R. and Couto, A. B.: The multi-viewing multi-
channel multi-polarisation imager – Overview of the 3MI polarimetric mission for aerosol and cloud characterization, J. Quant.
Spectrosc. Radiat. Transf., 219, 23–32, doi:10.1016/j.jqsrt.2018.07.008, 2018.

Frouin, R. J., Franz, B. A., Ibrahim, A., Knobelspiesse, K., Ahmad, Z., Cairns, B., Chowdhary, J., Dierssen, H. M., Tan, J.,

840   Dubovik, O., Huang, X., Davis, A. B., Kalashnikova, O., Thompson, D. R., Remer, L. A., Boss, E., Coddington, O.,
Deschamps, P.-Y., Gao, B.-C., Gross, L., Hasekamp, O., Omar, A., Pelletier, B., Ramon, D., Steinmetz, F. and Zhai, P.-W.:
Atmospheric Correction of Satellite Ocean-Color Imagery During the PACE Era, Front. Earth Sci., 7(July), 1–43,
doi:10.3389/feart.2019.00145, 2019.

Fu, G., Hasekamp, O., Rietjens, J., Smit, M., Di Noia, A., Cairns, B., Wasilewski, A., Diner, D., Seidel, F., Xu, F.,

845   Knobelspiesse, K., Gao, M., da Silva, A., Burton, S., Hostetler, C., Hair, J. and Ferrare, R.: Aerosol retrievals from different
polarimeters during the ACEPOL campaign using a common retrieval algorithm, Atmos. Meas. Tech., 13(2), 553–573,
doi:10.5194/amt-13-553-2020, 2020.

Goloub, P., Tanré, D., Deuzé, J. L., Herman, M., Marchand, A. and Bréon, F. M.: Validation of the first algorithm applied for deriving the aerosol properties over the ocean using the polder/adeos measurements, IEEE Trans. Geosci. Remote Sens., 37(3 II), 1575–1585, doi:10.1109/36.763268, 1999.

Hair, J. W., Hostetler, C. A., Cook, A. L., Harper, D. B., Ferrare, R. A., Mack, T. L., Welch, W., Izquierdo, L. R. and Hovis, F. E.: Airborne High Spectral Resolution Lidar for profiling aerosol optical properties, Appl. Opt., 47(36), 6734, doi:10.1364/AO.47.006734, 2008.

Hansen, J., Sato, M., Kharecha, P. and Von Schuckmann, K.: Earth's energy imbalance and implications, Atmos. Chem. Phys., 11(24), 13421–13449, doi:10.5194/acp-11-13421-2011, 2011.

Hasekamp, O., Tuinder, O. and Stammes, P.: Final report of the O3M-SAF activity: Aerosol retrieval from GOME-2: Improving computational efficiency and first application, [online] Available from: http://o3msaf.fmi.fi/docs/vs/2008/Hasekamp_final_report.pdf, 2008.

Hasekamp, O. P. and Landgraf, J.: Retrieval of aerosol properties over land surfaces: capabilities of multiple-viewing-angle intensity and polarization measurements, Appl. Opt., 46(16), 3332, doi:10.1364/AO.46.003332, 2007.

Hobbs, P. V: Aerosol-cloud-climate interactions, Academic Press., 1993.

Holben, B. N., Eck, T. F., Slutsker, I., Tanré, D., Buis, J. P., Setzer, A., Vermote, E., Reagan, J. A., Kaufman, Y. J., Nakajima, T., Lavenu, F., Jankowiak, I. and Smirnov, A.: AERONET—A Federated Instrument Network and Data Archive for Aerosol Characterization, Remote Sens. Environ., 66(1), 1–16, doi:10.1016/S0034-4257(98)00031-5, 1998.

Holben, B. N., Tanré, D., Smirnov, A., Eck, T. F., Slutsker, I., Abuhassan, N., Newcomb, W. W., Schafer, J. S., Chatenet, B., Lavenu, F., Kaufman, Y. J., Castle, J. Vande, Setzer, A., Markham, B., Clark, D., Frouin, R., Halthore, R., Karneli, A., O'Neill, N. T., Pietras, C., Pinker, R. T., Voss, K. and Zibordi, G.: An emerging ground-based aerosol climatology: Aerosol optical depth from AERONET, J. Geophys. Res. Atmos., 106(D11), 12067–12097, doi:10.1029/2001JD900014, 2001.

Hovenier, J. W., Van Der Mee, C. and Domke, H.: Transfer of Polarized Light in Planetary Atmospheres, Springer Netherlands, Dordrecht., 2004.

Kahn, R. A., Nelson, D. L., Garay, M. J., Levy, R. C., Bull, M. A., Diner, D. J., Martonchik, J. V., Paradise, S. R., Hansen, E. G. and Remer, L. A.: MISR Aerosol Product Attributes and Statistical Comparisons With MODIS, IEEE Trans. Geosci. Remote Sens., 47(12), 4095–4114, doi:10.1109/TGRS.2009.2023115, 2009.

Kahn, R. A., Gaitley, B. J., Garay, M. J., Diner, D. J., Eck, T. F., Smirnov, A. and Holben, B. N.: Multiangle Imaging SpectroRadiometer global aerosol product assessment by comparison with the Aerosol Robotic Network, J. Geophys. Res. Atmos., 115(23), doi:10.1029/2010JD014601, 2010.

Kahnert, M.: On the discrepancy between modeled and measured mass absorption cross sections of light absorbing carbon aerosols, Aerosol Sci. Technol., 44(6), 453–460, doi:10.1080/02786821003733834, 2010.

Kaufman, Y. J., Tanré, D. and Boucher, O.: A satellite view of aerosols in the climate system., Nature, 419(6903), 215–223, doi:10.1038/nature01091, 2002.

Kawata, Y., Yamazaki, A., Kusaka, T. and Information, E.: Multiple Scattering Computations in an Atmosphere-Ocean System

with an Anisotropic Cox-Munk Surface Model, , (1985), 1123–1125, 1995.

Knobelspiesse, K., Tsigaridis, K., Cairns, B., Chowdhary, J., Mishchenko, M., van Diedenhoven, B., Ottaviani, M., Alexandrov, M. and Martin, W.: Analysis of fine-mode aerosol retrieval capabilities by different passive remote sensing instrument designs, Opt. Express, 20(19), 21457, doi:10.1364/oe.20.021457, 2012.

Knobelspiesse, K. D., Barbosa, H., Hair, J. W., Harper, D. B., Hostetler, C. A., Maring, H., Mcbride, B., Norlin, K. A. and Tan, Q.: The Aerosol Characterization from Polarimeter and Lidar (ACEPOL) airborne field campaign, Earth Syst. Sci. Data(in Prep., 2020.

Kokhanovsky, A. A., Davis, A. B., Cairns, B., Dubovik, O., Hasekamp, O. P., Sano, I., Mukai, S., Rozanov, V. V., Litvinov, P., Lapyonok, T., Kolomiets, I. S., Oberemok, Y. A., Savenkov, S., Martin, W., Wasilewski, A., Di Noia, A., Stap, F. A., Rietjens, J., Xu, F., Natraj, V., Duan, M., Cheng, T. and Munro, R.: Space-based remote sensing of atmospheric aerosols: The multi-angle spectro-polarimetric frontier, Earth-Science Rev., 145, 85–116, doi:10.1016/j.earscirev.2015.01.012, 2015.

Koren, I., Kaufman, Y. J., Remer, L. A. and Martins, J. V.: Measurement of the Effect of Amazon Smoke on Inhibition of Cloud Formation, Science (80-.)., 303(5662), 1342–1345, doi:10.1126/science.1089424, 2004.

Lenoble, J., Herman, M., Deuzé, J. L., Lafrance, B., Santer, R. and Tanré, D.: A successive order of scattering code for solving the vector equation of transfer in the earth's atmosphere with aerosols, J. Quant. Spectrosc. Radiat. Transf., 107(3), 479–507, doi:10.1016/j.jqsrt.2007.03.010, 2007.

Lenoble, J., Remer, L. and Tanré, D.: Aerosol Remote Sensing, edited by J. Lenoble, L. Remer, and D. Tanre, Springer Berlin Heidelberg, Berlin, Heidelberg., 2013.

Leroy, M., Deuzé, J. L., Bréon, F. M., Hautecoeur, O., Herman, M., Buriez, J. C., Tanré, D., Bouffiès, S., Chazette, P. and Roujean, J. L.: Retrieval of atmospheric properties and surface bidirectional reflectances over land from POLDER/ADEOS, J. Geophys. Res. Atmos., 102(D14), 17023–17037, doi:10.1029/96JD02662, 1997.

Levy, R. C., Mattoo, S., Munchak, L. A., Remer, L. A., Sayer, A. M., Patadia, F. and Hsu, N. C.: The Collection 6 MODIS aerosol products over land and ocean, Atmos. Meas. Tech., 6(11), 2989–3034, doi:10.5194/amt-6-2989-2013, 2013.

Li, L., Dubovik, O., Derimian, Y., Schuster, G. L., Lapyonok, T., Litvinov, P., Ducos, F., Fuertes, D., Chen, C., Li, Z., Lopatin, A., Torres, B. and Che, H.: Retrieval of aerosol components directly from satellite and ground-based measurements, Atmos. Chem. Phys., 19(21), 13409–13443, doi:10.5194/acp-19-13409-2019, 2019.

Limbacher, J. A. and Kahn, R. A.: Updated MISR over-water research aerosol retrieval algorithm - Part 2: A multi-angle aerosol retrieval algorithm for shallow, turbid, oligotrophic, and eutrophic waters, Atmos. Meas. Tech., 12(1), 675–689, doi:10.5194/amt-12-675-2019, 2019.

Litvinov, P., Hasekamp, O. and Cairns, B.: Models for surface reflection of radiance and polarized radiance: Comparison with airborne multi-angle photopolarimetric measurements and implications for modeling top-of-atmosphere measurements, Remote Sens. Environ., 115(2), 781–792, doi:10.1016/j.rse.2010.11.005, 2011.

Mack, L. A., Levin, E. J. T., Kreidenweis, S. M., Obrist, D., Moosmüller, H., Lewis, K. A., Arnott, W. P., McMeeking, G. R., Sullivan, A. P., Wold, C. E., Hao, W.-M., Collett, J. L. and Malm, W. C.: Optical closure experiments for biomass smoke

aerosols, Atmos. Chem. Phys., 10(18), 9017–9026, doi:10.5194/acp-10-9017-2010, 2010.

Maignan, F., Bréon, F. M. and Lacaze, R.: Bidirectional reflectance of Earth targets: Evaluation of analytical models using a large set of spaceborne measurements with emphasis on the Hot Spot, Remote Sens. Environ., 90(2), 210–220, doi:10.1016/j.rse.2003.12.006, 2004.

920 Maignan, F., Bréon, F. M., Fédèle, E. and Bouvier, M.: Polarized reflectances of natural surfaces: Spaceborne measurements and analytical modeling, Remote Sens. Environ., 113(12), 2642–2650, doi:10.1016/j.rse.2009.07.022, 2009.

Manfred, K. M., Washenfelder, R. A., Wagner, N. L., Adler, G., Erdesz, F., Womack, C. C., Lamb, K. D., Schwarz, J. P., Franchin, A., Selimovic, V., Yokelson, R. J. and Murphy, D. M.: Investigating biomass burning aerosol morphology using a laser imaging nephelometer, Atmos. Chem. Phys., 18(3), 1879–1894, doi:10.5194/acp-18-1879-2018, 2018.

925 Martins, J. V., Hobbs, P. V., Weiss, R. E. and Artaxo, P.: Sphericity and morphology of smoke particles from biomass burning in Brazil, J. Geophys. Res. Atmos., 103(D24), 32051–32057, doi:10.1029/98JD01153, 1998.

Martins, J. V., Fernandez-Borda, R., McBride, B., Remer, L. and Barbosa, H. M. J.: The harp hyperangular imaging polarimeter and the need for small satellite payloads with high science payoff for earth science remote sensing, in International Geoscience and Remote Sensing Symposium (IGARSS), vol. 2018-July, pp. 6304–6307, IEEE., 2018.

930 Martonchik, J. V., Diner, D. J., Crean, K. A. and Bull, M. A.: Regional aerosol retrieval results from MISR, IEEE Trans. Geosci. Remote Sens., 40(7), 1520–1531, doi:10.1109/TGRS.2002.801142, 2002.

Masmoudi, M., Chaabane, M., Tanré, D., Gouloup, P., Blarel, L. and Elleuch, F.: Spatial and temporal variability of aerosol: Size distribution and optical properties, Atmos. Res., 66(1–2), 1–19, doi:10.1016/S0169-8095(02)00174-6, 2003.

Mcbride, B. A., Martins, J. V., Barbosa, H. M. J. and Birmingham, W.: Spatial distribution of cloud droplet size properties 935 from Airborne Hyper-Angular Rainbow Polarimeter (AirHARP) measurements, , (March), 2020.

McGill, M., Hlavka, D., Hart, W., Scott, V. S., Spinhirne, J. and Schmid, B.: Cloud Physics Lidar: instrument description and initial measurement results, Appl. Opt., 41(18), 3725, doi:10.1364/ao.41.003725, 2002.

Mischenko, M., Travis, L. D. L., Lacis, A. A., Mishchenko, M. I., Travis, L. D. L. and Lacis, A. A.: Scattering, absorption, and emission of light by small particles, NASA Goddard Inst. Sp. Stud., 1–128, 2002.

940 Mishchenko, M. I. and Travis, L. D.: Satellite retrieval of aerosol properties over the ocean using polarization as well as intensity of reflected sunlight, J. Geophys. Res., 102(D12), 16989, doi:10.1029/96JD02425, 1997.

Moosmüller, H., Varma, R. and Arnott, W. P.: Cavity Ring-Down and Cavity-Enhanced Detection Techniques for the Measurement of Aerosol Extinction, Aerosol Sci. Technol., 39(1), 30–39, doi:10.1080/027868290903880, 2005.

Nicolae, D., Nemuc, A., Müller, D., Talianu, C., Vasilescu, J., Belegante, L. and Kolgotin, A.: Characterization of fresh and 945 aged biomass burning events using multiwavelength Raman lidar and mass spectrometry, J. Geophys. Res. Atmos., 118(7), 2956–2965, doi:10.1002/jgrd.50324, 2013.

Patadia, F., Levy, R. C. and Mattoo, S.: Correcting for trace gas absorption when retrieving aerosol optical depth from satellite observations of reflected shortwave radiation, Atmos. Meas. Tech., 11(6), 3205–3219, doi:10.5194/amt-11-3205-2018, 2018.

Penner, J. E., Andreae, M. O., Annegarn, H., Barrie, L., Feichter, J., Hegg, D., Jayaraman, A., Leaitch, R., Murphy, D., Nganga,

950   J. and others: Aerosols, their direct and indirect effects, in Climate Change 2001: The Scientific Basis. Contribution of Working Group I to the Third Assessment Report of the Intergovernmental Panel on Climate Change, pp. 289–348, Cambridge University Press., 2001.

Penner, J. E., Xu, L. and Wang, M.: Satellite methods underestimate indirect climate forcing by aerosols, Proc. Natl. Acad. Sci., 108(33), 13404–13408, doi:10.1073/pnas.1018526108, 2011.

955   Petzold, A., Schloesser, H., Sheridan, P. J., Arnott, W. P., Ogren, J. A. and Virkkula, A.: Evaluation of multiangle absorption photometry for measuring aerosol light absorption, Aerosol Sci. Technol., 39(1), 40–51, doi:10.1080/027868290901945, 2005.

Phillips, D. L.: A technique for the numerical solution of certain integral equations of the first kind, J. ACM, 9(1), 84–97, 1962.

Poudel, S., Flurchick, K., Smith, D., Bililign, S. and Fiddler, M.: Optical Properties of Biomass Burning Aerosols: Comparison
960   of Experimental Measurements and T-Matrix Calculations, Atmosphere (Basel)., 8(12), 228, doi:10.3390/atmos8110228, 2017.

Rahman, H., Pinty, B. and Verstraete, M. M.: Coupled Surface-Atmosphere Reflectance (CSAR) Model Very High Resolution Radiometer Data, J. Geophys. Res., 98(93), 20,791-20,801, 1993.

Remer, L. A., Knobelspiesse, K., Zhai, P., Xu, F., Kalashnikova, O. V., Chowdhary, J., Hasekamp, O., Dubovik, O., Wu, L.,
965   Ahmad, Z., Boss, E., Cairns, B., Coddington, O., Davis, A. B., Dierssen, H. M., Diner, D. J., Franz, B., Frouin, R., Gao, B., Ibrahim, A., Levy, R. C., Martins, J. V., Omar, A. H. and Torres, O.: Retrieving Aerosol Characteristics From the PACE Mission, Part 2: Multi-Angle and Polarimetry, Front. Environ. Sci., 7(July), 1–21, doi:10.3389/fenvs.2019.00094, 2019.

Rocha-Lima, A., Martins, J. V., Remer, L. A., Krotkov, N. A., Tabacniks, M. H., Ben-Ami, Y. and Artaxo, P.: Optical, microphysical and compositional properties of the Eyjafjallajökull volcanic ash, Atmos. Chem. Phys., 14(19), 10649–10661,
970   doi:10.5194/acp-14-10649-2014, 2014.

Román, R., Benavent-Oltra, J. A., Casquero-Vera, J. A., Lopatin, A., Cazorla, A., Lyamani, H., Denjean, C., Fuertes, D., Pérez-Ramírez, D., Torres, B., Toledano, C., Dubovik, O., Cachorro, V. E., de Frutos, A. M., Olmo, F. J. and Alados-Arboledas, L.: Retrieval of aerosol profiles combining sunphotometer and ceilometer measurements in GRASP code, Atmos. Res., 204(February), 161–177, doi:10.1016/j.atmosres.2018.01.021, 2018.

975   Roujean, J.-L., Leroy, M. and Deschamps, P.-Y.: A bidirectional reflectance model of the Earth's surface for the correction of remote sensing data, J. Geophys. Res., 97(D18), 20455, doi:10.1029/92JD01411, 1992.

Sayer, A. M., Hsu, N. C., Bettenhausen, C. and Jeong, M. J.: Validation and uncertainty estimates for MODIS Collection 6 "deep Blue" aerosol data, J. Geophys. Res. Atmos., 118(14), 7864–7872, doi:10.1002/jgrd.50600, 2013.

Schott, J. R.: Fundamentals of Polarimetric Remote Sensing, Society of Photo Optical. [online] Available from:
980   https://books.google.com/books?id=-2V0gAJ3aG4C, 2009.

Schuster, G., Espinosa, W., Ziemba, L., Beyersdorf, A., Rocha-Lima, A., Anderson, B., Martins, J., Dubovik, O., Ducos, F., Fuertes, D., Lapyonok, T., Shook, M., Derimian, Y., Moore, R., Schuster, G. L., Espinosa, W. R., Ziemba, L. D., Beyersdorf, A. J., Rocha-Lima, A., Anderson, B. E., Martins, J. V., Dubovik, O., Ducos, F., Fuertes, D., Lapyonok, T., Shook, M.,

Derimian, Y. and Moore, R. H.: A Laboratory Experiment for the Statistical Evaluation of Aerosol Retrieval (STEAR)
985   Algorithms., 2019.

Shiraiwa, M., Ueda, K., Pozzer, A., Lammel, G., Kampf, C. J., Fushimi, A., Enami, S., Arangio, A. M., Fröhlich-Nowoisky,
J., Fujitani, Y., Furuyama, A., Lakey, P. S. J., Lelieveld, J., Lucas, K., Morino, Y., Pöschl, U., Takahama, S., Takami, A.,
Tong, H., Weber, B., Yoshino, A. and Sato, K.: Aerosol Health Effects from Molecular to Global Scales, Environ. Sci.
Technol., 51(23), 13545–13567, doi:10.1021/acs.est.7b04417, 2017.

990   Smit, J. M., Rietjens, J. H. H., van Harten, G., Di Noia, A., Laauwen, W., Rheingans, B. E., Diner, D. J., Cairns, B., Wasilewski,
A., Knobelspiesse, K. D., Ferrare, R. and Hasekamp, O. P.: SPEX airborne spectropolarimeter calibration and performance,
Appl. Opt., 58(21), 5695, doi:10.1364/AO.58.005695, 2019.

Snider, G., Weagle, C. L., Martin, R. V, Van Donkelaar, A., Conrad, K., Cunningham, D., Gordon, C., Zwicker, M., Akoshile,
C., Artaxo, P., Anh, N. X., Brook, J., Dong, J., Garland, R. M., Greenwald, R., Griffith, D., He, K., Holben, B. N., Kahn, R.,
995   Koren, I., Lagrosas, N., Lestari, P., Ma, Z., Vanderlei Martins, J., Quel, E. J., Rudich, Y., Salam, A., Tripathi, S. N., Yu, C.,
Zhang, Q., Zhang, Y., Brauer, M., Cohen, A., Gibson, M. D. and Liu, Y.: SPARTAN: A global network to evaluate and
enhance satellite-based estimates of ground-level particulate matter for global health applications, Atmos. Meas. Tech., 8(1),
505–521, doi:10.5194/amt-8-505-2015, 2015.

Sun, W. and Lukashin, C.: Modeling polarized solar radiation from the ocean-atmosphere system for CLARREO inter-
1000   calibration applications, Atmos. Chem. Phys., 13(20), 10303–10324, doi:10.5194/acp-13-10303-2013, 2013.

Tanré, D., Bräon, F. M., Deuzä, J. L., Dubovik, O., Ducos, F., Franäois, P., Goloub, P., Herman, M., Lifermann, A. and
Waquet, F.: Remote sensing of aerosols by using polarized, directional and spectral measurements within the A-Train: The
PARASOL mission, Atmos. Meas. Tech., 4(7), 1383–1395, doi:10.5194/amt-4-1383-2011, 2011.

Tikhonov, A. N.: Regularization of incorrectly posed problems, in Soviet Mathematics Doklady, vol. 4, pp. 1624–1627., 1963.
1005   Titos, G., Ealo, M., Román, R., Cazorla, A., Sola, Y., Dubovik, O., Alastuey, A. and Pandolfi, M.: Retrieval of aerosol
properties from ceilometer and photometer measurements: long-term evaluation with in-situ data and statistical analysis at
Montsec (southern Pyrenees), Atmos. Meas. Tech. Discuss., 1–23, doi:10.5194/amt-2018-431, 2019.

Torres, B., Dubovik, O., Fuertes, D., Schuster, G., Eugenia Cachorro, V., Lapyonok, T., Goloub, P., Blarel, L., Barreto, A.,
Mallet, M., Toledano, C. and Tanré, D.: Advanced characterisation of aerosol size properties from measurements of spectral
1010   optical depth using the GRASP algorithm, Atmos. Meas. Tech., 10(10), 3743–3781, doi:10.5194/amt-10-3743-2017, 2017.

Wang, J., Xu, X., Ding, S., Zeng, J., Spurr, R., Liu, X., Chance, K. and Mishchenko, M.: A numerical testbed for remote
sensing of aerosols, and its demonstration for evaluating retrieval synergy from a geostationary satellite constellation of GEO-
CAPE and GOES-R, J. Quant. Spectrosc. Radiat. Transf., 146, 510–528, doi:10.1016/j.jqsrt.2014.03.020, 2014.

Wanner, W., Li, X. and Strahler, a H.: Kernel-driven models for the bidirectional reflectance dis- contain only geometric
1015   terms but no physical parameters . function land surfaces attempt The complete model then is linear be scaled to ar- to describe
the BRDF as a linear superposition of a set, J. Geophys. Res., 100(D10), 21077–21089 [online] Available from:
http://www.agu.org/pubs/crossref/1995/95JD02371.shtml, 1995.

Welton, E. J., Campbell, J. R., Spinhirne, J. D. and Scott III, V. S.: Global monitoring of clouds and aerosols using a network of micropulse lidar systems, Lidar Remote Sens. Ind. Environ. Monit., 4153(February 2001), 151, doi:10.1117/12.417040, 2001.

Werdell, P. J., Behrenfeld, M. J., Bontempi, P. S., Boss, E., Cairns, B., Davis, G. T., Franz, B. A., Gliese, U. B., Gorman, E. T., Hasekamp, O., Knobelspiesse, K. D., Mannino, A., Martins, J. V., McClain, C. R., Meister, G. and Remer, L. A.: The Plankton, Aerosol, Cloud, Ocean Ecosystem Mission: Status, Science, Advances, Bull. Am. Meteorol. Soc., 100(9), 1775–1794, doi:10.1175/BAMS-D-18-0056.1, 2019.

Westberry, T. K., Shi, Y. R., Yu, H., Behrenfeld, M. J. and Remer, L. A.: Satellite-detected Ocean Ecosystem Response to Volcanic Eruptions in the Subarctic Northeast Pacific Ocean, Geophys. Res. Lett., 1–11, doi:10.1029/2019gl083977, 2019.

Xu, X. and Wang, J.: Retrieval of aerosol microphysical properties from AERONET photopolarimetric measurements: 1. Information content analysis, J. Geophys. Res. Atmos., 120(14), 7059–7078, doi:10.1002/2015JD023108, 2015.

Xu, X. and Wang, J.: UNL-VRTM, A Testbed for Aerosol Remote Sensing: Model Developments and Applications, in Springer Series in Light Scattering: Volume 4: Light Scattering and Radiative Transfer, edited by A. Kokhanovsky, pp. 1–69, Springer International Publishing, Cham., 2019.